Spine-neck geometry determines NMDA receptor–dependent Ca^{2+} signaling in dendrites

Jun Noguchi

DOCTOR OF PHILOSOPHY

Department of Physiological Science
School of Life Science
The Graduate University for Advanced Studies

2004

CONTENTS

Page

Summary -- 3

Introduction -- 4

Materials and Methods -- 6

Results -- 12

Discussion -- 39

Appendix -- 53

Acknowledgement -- 61

References -- 62

Summary

Increases in cytosolic Ca^{2+} concentration ($[Ca^{2+}]_i$) mediated by NMDA-sensitive glutamate receptors (NMDARs) are important for synaptic plasticity. We studied a wide variety of dendritic spines on rat CA1 pyramidal neurons in acute hippocampal slices. Two-photon uncaging and Ca^{2+} imaging revealed that NMDAR-mediated currents increased with spine-head volume and that even the smallest spines contained a significant number of NMDARs. The fate of Ca^{2+} that entered spine heads through NMDARs was governed by the shape (length and radius) of the spine neck. Larger spines had necks that permitted greater efflux of Ca^{2+} into the dendritic shaft, whereas smaller spines manifested a larger increase in $[Ca^{2+}]_i$ within the spine compartment as a result of a smaller Ca^{2+} flux through the neck. Spine-neck geometry is thus an important determinant of spine Ca^{2+} signaling, allowing small spines to be the preferential sites for isolated induction of long-term potentiation.

Introduction

Glutamate receptors sensitive to *N*-methyl-D-aspartate (NMDA) mediate increases in the intracellular free Ca^{2+} concentration ($[Ca^{2+}]_i$) of neurons that lead to bidirectional regulation of synaptic plasticity (Lisman, 1989;Shouval et al., 2002), which supports self-organization of neuronal networks in the central nervous system (Lisman, 2003;Mori and Mishina, 2003;Nakazawa et al., 2004). Synaptic functions and plasticity have been proposed to be dependent on synaptic structure (Bonhoeffer and Yuste, 2002;Harris et al., 2003;Kasai et al., 2003). With the use of two-photon photolysis of caged glutamate, we previously showed that spine-head volume is an important determinant of the expression of α-amino-3-hydroxy-5-methyl-4-isoxazolepropionate (AMPA)–sensitive glutamate receptors (Matsuzaki et al., 2001), which mediate fast glutamatergic synaptic transmission. We recently applied the same approach to induce NMDA receptor (NMDAR)–dependent long-term plasticity at visually selected single spines; this plasticity was dependent on spine-head volume and was induced more efficiently in smaller spines than in larger ones (Matsuzaki et al., 2004). However, the dependence of NMDAR-mediated Ca^{2+} signaling on spine structure has not been clarified, given that selective stimulation of the single presynaptic fibers that innervate identified spines has been difficult to achieve electrically because of the spread of the electric current.

The role of diverse spine-neck structures in the regulation of neuronal signaling is also unclear (Rall, 1970;Svoboda et al., 1996;Shepherd, 1996). In particular, it remains unknown whether spine necks allow outflow of Ca^{2+} into the dendritic shaft (Helmchen, 2002). Although some studies have predicted outflow of Ca^{2+} from spine heads into the dendritic shaft (Majewska et al., 2000a;Holthoff et al., 2002;Korkotian et al., 2004), it has been claimed that such outflow is attributable mostly to the buffering action of the large concentrations of the Ca^{2+} indicator dyes used for Ca^{2+} measurement in these studies (Sabatini et al., 2002).

We have now used two-photon photolysis of a caged-glutamate compound (MNI-glutamate) (Matsuzaki et al., 2001) to achieve three-dimensionally confined application of glutamate at single spine heads or across the dendritic surface of CA1 pyramidal neurons in acute hippocampal slices . We combined this approach with two-photon Ca^{2+} imaging and whole-cell patch-clamp recording to monitor the activation of NMDARs in these neurons with a high spatial resolution. A low-affinity Ca^{2+} indicator was used to minimize the perturbation of endogenous Ca^{2+}-buffering capacity. We investigated NMDAR-mediated Ca^{2+} signaling in various types of spines and found that spine-head volume was negatively correlated with spine $[Ca^{2+}]_i$ but positively correlated with $[Ca^{2+}]_i$ of the dendritic shaft at the base of the spine neck. These data suggest that the spine neck is a critical determinant of spine Ca^{2+} signaling and enables small spines to be the preferential sites of induction and consolidation of long-term structural plasticity. We provide a simple, quantitative model of spine Ca^{2+} signaling to account for the function of spine necks.

Materials and Methods

Preparations

Hippocampal slices with a thickness of 350 µm were prepared from 15- to 22-day-old Sprague-Dawley rats (Matsuzaki et al., 2001). Slices were transferred individually to a recording chamber that was superfused with a solution containing 125 mM NaCl, 2.5 mM KCl, 1 mM $MgCl_2$, 2 mM $CaCl_2$, 1.25 mM NaH_2PO_4, 26 mM $NaHCO_3$, and 20 mM D-glucose, which was bubbled with 95% O_2 and 5% CO_2 gas. The bathing solution also contained 1 µM tetrodotoxin (Seikagaku, Tokyo, Japan), 50 µM picrotoxin (Wako, Osaka, Japan), 200 µM Trolox (Aldrich, Milwaukee, WI), and 200 µM (*S*)-a-methyl-4-carboxyphenylglycine (MCPG) (Tocris, Bristol, UK). For recording of NMDAR-mediated current, the $MgCl_2$ concentration of the bathing solution was reduced to 0.05 mM and 10 µM 6-cyano-7-nitroquinoxaline-2,3-dione (CNQX) (Sigma, St. Louis, MO) was added. For recording of AMPAR-mediated current, 100 µM D,L-2-amino-5-phosphonovaleric acid (APV) (Tocris) was included in the bathing solution. Whole-cell patch pipettes were filled with a solution containing 130 mM cesium gluconate, 4 mM $MgCl_2$, 4 mM ATP (sodium salt), 0.4 mM GTP (sodium salt), 10 mM disodium phosphocreatine (Sigma), 10 mM HEPES-CsOH (pH 7.2), 0.5 mM OGB-5N, and 0.04 mM Alexa Fluor 594 (Molecular Probes, Eugene, OR). We studied mostly the third or fourth branches of dendrites. All physiological experiments were performed at room temperature (23° to 25°C), unless otherwise noted. The experiments were approved by the Animal Experiment Committee of the National Institute for Physiological Sciences.

Two-photon excitation imaging and uncaging of MNI-glutamate

Time-lapse two-photon imaging of dendritic spines was performed with an upright microscope (BX50WI; Olympus, Tokyo, Japan) equipped with a water-immersion objective lens (LUMPlanFI/IR 60×, numerical aperture of 0.9) and with a self-made program based on LabView (National Instruments, Austin, TX). Two mode-locked femtosecond-pulse Ti:sapphire lasers (Tsunami; Spectra Physics, Mountain View, CA) set at wavelengths of 720 and 830 nm were connected to the laser-scanning microscope via two independent scan-heads. For imaging of dendritic spines, we used the laser set at the wavelength of 830 nm; the point-spread function of the focal volume was estimated with the use of 0.1-µm fluorescent beads as 0.43 µm (FWHM) laterally and 1.8 µm axially. For three-dimensional reconstruction, 41 *xy*-images separated by 0.2 µm were stacked by summation of fluorescence values at each pixel. Immediately before two-photon uncaging of MNI-glutamate, one image was acquired at the wavelength of 830 nm for precise adjustment of the point of photolysis; MNI-glutamate (10 mM) was then applied locally from a glass pipette positioned close to the selected dendrite. We chose a duration of irradiation of 5 ms, given that radiation-induced damage caused by the multiphoton effect is reduced by the use of a lower laser power for a longer duration and that this approach did not much reduce the spatial resolution of NMDAR activation (see below). The irradiation was gated by a mechanical shutter (Uniblitz, Rochester, NY). The average power of the uncaging laser was set to ~ 3 mW.

Calcium imaging was based on the OGB-5N/Alexa Fluor 594 fluorescence ratio (R). Fluorescence emission was acquired at 400 to 570 nm (green channel) and 590 to 650 nm (red channel) for OGB-5N and Alexa Fluor 594, respectively. Fluorescence of OGB-5N and Alexa Fluor 594 contributed less than 1% to the total fluorescence of the red and green channels, respectively, in our recording conditions. Background levels of Alexa Fluor 594 and OGB-5N fluorescence were obtained from the same image and were subtracted from specific signals. We performed in situ calibration of R by whole-cell perfusion with internal solutions containing 10 mM EGTA or 10 mM Ca^{2+}, which provided estimates of R_{min} and R_{max} as 0.112 and 1.176. Given that R before stimulation (R_0) was similar to R_{min}, we used the relation $?R = R - R_0$ to estimate $[Ca^{2+}]_i$ in micromolar as $32 \times ?R/(1.1 - ?R) = K_{Ca}(R - R_{min})/(R_{max} - R)$, assuming the affinity (K_{Ca}) of OGB-5N for Ca^{2+} to be 32 µM (DiGregorio and Vergara, 1997). We started imaging roughly 30 min after whole-cell perfusion, when the fluorescence intensity had reached its plateau value. Throughout the recording period for more than 1 hr, we detected neither significant change in the resting $[Ca^{2+}]_i$ nor increase in the decay time constants of NMDAR-mediated Ca^{2+} transients in spine heads (30–220 ms).

Electrophysiology

Neurons were voltage-clamped at –70 mV, and the currents were low-pass filtered at 2 kHz and sampled at 50 kHz. Series resistance was 15.4 ± 4.0 MΩ (mean ± SD). Three-dimensional mapping of AMPARs was performed as described (Matsuzaki et al., 2001). Uncaging was performed at a laser power of 6 mW and a duration of 0.6 ms. The *xy* scanning of a region of interest (ROI) comprising 16 by 16 pixels (1 pixel = 0.33 μm) was performed at four to six different *z*-axis planes each separated by 1 μm. A pseudorandom sequence of scanning of pixels in an ROI was constructed to ensure that the distance between two successive pixels was >2.5 to 5 μm and that AMPA currents were sampled at an interval of 100 ms. Peak amplitudes of AMPA currents were assigned to each pixel, linear-interpolated, stacked along the *z*-axis by the maximum-intensity method, and displayed with a pseudocolor coding (Figures 9A and 9B).

The spatial distribution of glutamate, $G(x,z,t)$, after uncaging was numerically obtained with the use of Mathematica5.0 (Wolfram Research, Champaign, IL) as described (Matsuzaki et al., 2001), assuming σ_x and σ_z to be 0.167 and 0.547 μm, respectively. From $G(x,z,t)$, the opening probability of NMDARs, $NMDAR(x,z,t)$, can be obtained with the kinetic model of NMDARs (Lester et al., 1993). The peak amplitudes of $NMDAR(x,z,t)$ were calculated at various x and z values, allowing estimation of lateral and axial spread of activation of NMDARs in terms of FWHM diameters as 1.4 and 2.2 μm, respectively. Our simulation and experiments indicated that a longer duration of laser irradiation (5 ms) did not substantially affect the spatial resolution of mapping of glutamate sensitivity if the total extent of uncaging was unchanged.

Spine geometries

We first calibrated the fluorescence of Alexa Fluor 594 in a volume of cytosol with the use of the largest spine in a dendritic region as described (Matsuzaki et al., 2004), assuming that Alexa Fluor 594 homogeneously filled the volume of dendrites and σ_x and σ_z to be 0.18 and 0.78 µm, respectively. In brief, the actual diameters of spines ($2r$) were estimated from the FWHM diameters with the use of the $2r$-FWHM relation for a sphere (See Appendix Figure 12A). If we assume a spherical spine head with a diameter of $2r_H$, we can obtain the conversion coefficient (k_F) from the fluorescence intensity in cytosolic volume with the equation $F_H = k_F(4/3)\pi r_H^3$. The conversion coefficient (k_F) was obtained for a dendritic region in each experiment. The diameter of dendritic shafts ($2r_D$) was also obtained from the $2r$-FWHM relation for a cylinder (Appendix Figure 12B). The diameter of dendritic shafts was variable (CV = 0.15) even within a given dendritic region (Figure 3A), and we obtained the average value for a dendrite within 0.5 µm of the base of the respective spine.

Spine-neck geometries were obtained for those spines whose necks were roughly parallel to the focal plane (Figure 6B). The length of the spine neck (l_N) was obtained from the fluorescence profile along the neck (Figure 6C). The spine head and dendritic shaft were fitted with Gaussian functions, and the edges of the spine neck were obtained with the use of the $2r$-FWHM relations (Figure 6C; Figure 12). A rectangular ROI (Figure 6C, box 1) was placed at the spine neck with a length and width sufficient to include the entire neck. The spine-neck fluorescence (F_N) was obtained from the fluorescence of four rectangular regions of identical size as follows: $F_N = F_1 - F_2 - F_3 + F_4$, where F_1, F_2, F_3, and F_4 represent fluorescence from the region containing the spine neck (Figure 6C, box 1), a region adjacent to the spine head (box 2) or to the nearby dendritic shaft (box 3), and a region separated from the dendrite (box 4), respectively. The diameter of the spine neck ($2r_N$) was obtained from the relation $F_N = k_F l_N \pi r_N^2$, with the use of the conversion coefficient obtained from a spherical spine in the same dendritic region (k_F) as described above. For those stubby spines whose neck structures were not well resolved, we assumed l_N as 0.05 µm and obtained r_N at the base of the spine adjacent to the outline of dendritic shaft.

Results

Ca^{2+} imaging with a dual-scanning two-photon microscope

We imaged CA1 pyramidal neurons clamped in the whole-cell mode with a solution containing the low-affinity Ca^{2+} indicator OregonGreen-BAPTA-5N (OGB-5N, 500 µM) and the Ca^{2+}-insensitive dye Alexa Fluor 594 (40 µM) (Figure 1A). These two dyes emit green and red fluorescence, respectively, but have broad two-photon absorption spectra that allow their simultaneous excitation at 830 nm (Sabatini et al., 2002). The $[Ca^{2+}]_i$ was determined ratiometrically from the fluorescence of both dyes (Figure 1B) in the presence of the AMPA receptor (AMPAR) blocker CNQX (10 µM), the metabotropic glutamate receptor blocker MCPG (200 µM), and Mg^{2+} (50 µM). Given that OGB-5N has a low affinity for Ca^{2+} (dissociation constant, 32 µM) (DiGregorio and Vergara, 1997) and its Ca^{2+} binding ratio (κ) is <15.6 (Neher and Augustine, 1992), it affects the intrinsic Ca^{2+} buffers of neurons only minimally. This value of κ is smaller than those for previous Ca^{2+}-imaging studies in pyramidal neurons (Helmchen et al., 1996;Majewska et al., 2000a;Sabatini et al., 2002) and therefore would be expected to have the least effect on the spatiotemporal pattern of Ca^{2+} signaling; we estimated the binding ratio of the intrinsic Ca^{2+} buffer to be 86 (see below). For simplicity, we assumed the resting $[Ca^{2+}]_i$ to be zero in the present study, given that OGB-5N does not allow precise measurement of $[Ca^{2+}]_i$ at values of <0.3 µM. The line for scanning was aligned with the axis of individual spines to monitor $[Ca^{2+}]_i$ in the spine head and at the base of the spine simultaneously

(Figure 1A). Alexa Fluor 594 fluorescence was also used for structural measurements.

Two-photon uncaging of MNI-glutamate (10 mM) was induced at the distal pole of a dendritic spine with a mode-locked Ti:sapphire laser (720 nm, 3 mW, 5 ms). This uncaging protocol was expected to induce currents with amplitudes about 2-3 times as large as those of miniature excitatory postsynaptic currents (EPSCs) (Matsuzaki et al., 2001). The NMDAR blocker APV (100 μM) eliminated both the increase in $[Ca^{2+}]_i$ ($\Delta[Ca^{2+}]_i$) and the whole-cell current induced by photolysis of MNI-glutamate (Figure 1C, 1D), indicating that the response was primarily mediated by NMDARs (Koester and Sakmann, 1998;Kovalchuk et al., 2000). The amplitude of $\Delta[Ca^{2+}]_i$ in the spine head often exceeded 10 μM (see Figure 3C), consistent with previous observations (Petrozzino et al., 1995). There was little delay between the onset of the NMDAR-mediated current and that of $\Delta[Ca^{2+}]_i$ in the spine head (Figure 1C), indicating that the NMDARs were present in the spines. The Ca^{2+} signals also indicated the absence of a large concentration of high-affinity Ca^{2+} buffers in pyramidal neurons, in contrast to cerebellar Purkinje neurons (Maeda et al., 1999).

The peak amplitudes of $\Delta[Ca^{2+}]_i$ and current varied markedly, with a coefficient of variation (CV) of ~0.3, as a result of the noise of recording and of channel gating (Figure 1E and 1F). The variability could be reduced to 0.11 to 0.21 by the averaging of three consecutive traces (Figure 1E and 1F), and we performed such averaging in all subsequent experiments. The peak $\Delta[\mathrm{Ca}^{2+}]_i$ in the spine head and the peak NMDAR-mediated current (I_{NMDA}) showed similar nonlinear dependence on the laser power at power values of <5 mW (Figure 1G), consistent with two-photon excitation of MNI-glutamate. The values of $\Delta[\mathrm{Ca}^{2+}]_i$ tended to saturate at laser powers of >5 mW, probably as a result of saturation of the activation of NMDARs in the single spines; the peak $\Delta[\mathrm{Ca}^{2+}]_i$ was in the range of 4 to 20 µM, which is less than the affinity of OGB-5N for Ca^{2+} (32 µM). In contrast, I_{NMDA} showed no apparent saturation (Figure 1G), probably as a result of the spillover of glutamate to surrounding dendritic structures (Rusakov and Kullmann, 1998). We therefore set the laser power to ~3 mW to minimize the spillover effect in all subsequent experiments. Such power was necessary to obtain an adequate signal-to-noise ratio for the NMDARs.

The spatial spread of activation of NMDARs was estimated by inducing sequential uncaging of MNI-glutamate at several points along the line connecting the distal tips of two neighboring spines separated by a distance of 2 µm (Figure 2A). The peaks of the maximal amplitudes of I_{NMDA} for the two spines were well separated (Figure 2B), and each peak was highly correlated with the $\Delta[\mathrm{Ca}^{2+}]_i$ for the respective spine. This result confirmed that NMDARs were selectively activated in single, isolated spines when uncaging was induced at the spine tip under our experimental conditions. The full-width at half-maximal (FWHM) resolution of I_{NMDA} thus estimated was ~1.4 µm, consistent with the prediction made from the established slow gating of NMDARs (Rusakov and Kullmann, 1998) (see Materials and Methods).

We found that the NMDAR-dependent increase in $[Ca^{2+}]_i$ in the dendritic shaft occurred with a delay of 5 to 30 ms for 90% of spines (*n* = 41) (Figure 1C), suggesting that Ca^{2+} that entered through NMDARs in the spine head spread into the dendritic shaft via the spine neck. Photolysis of MNI-glutamate at the dendritic shaft (Figure 2F) induced only small increases in $[Ca^{2+}]_i$ (*n* = 7) (Figures 2G and 2H), compared with those that were apparent with uncaging at the spine tip (Figure 2C–E). Increases in $[Ca^{2+}]_i$ were often undetectable (0.5 ± 0.5 µM, mean ± SD) when uncaging was effected at arbitrary points along the dendritic shaft at a distance of >2 µm from a neighboring spine, indicating that NMDARs were present in relatively small numbers on the dendritic shaft compared with the spine head, and that the $\Delta[Ca^{2+}]_i$ in shafts induced by two-photon uncaging of MNI-glutamate at isolated spine heads was attributable solely to Ca^{2+} efflux from those spine heads. The outflow of Ca^{2+} from spine to dendrite was considered physiological because it was similarly recorded at a temperature (32°C) higher than that (23° to 25°C) routinely used (*n* = 5, data not shown).

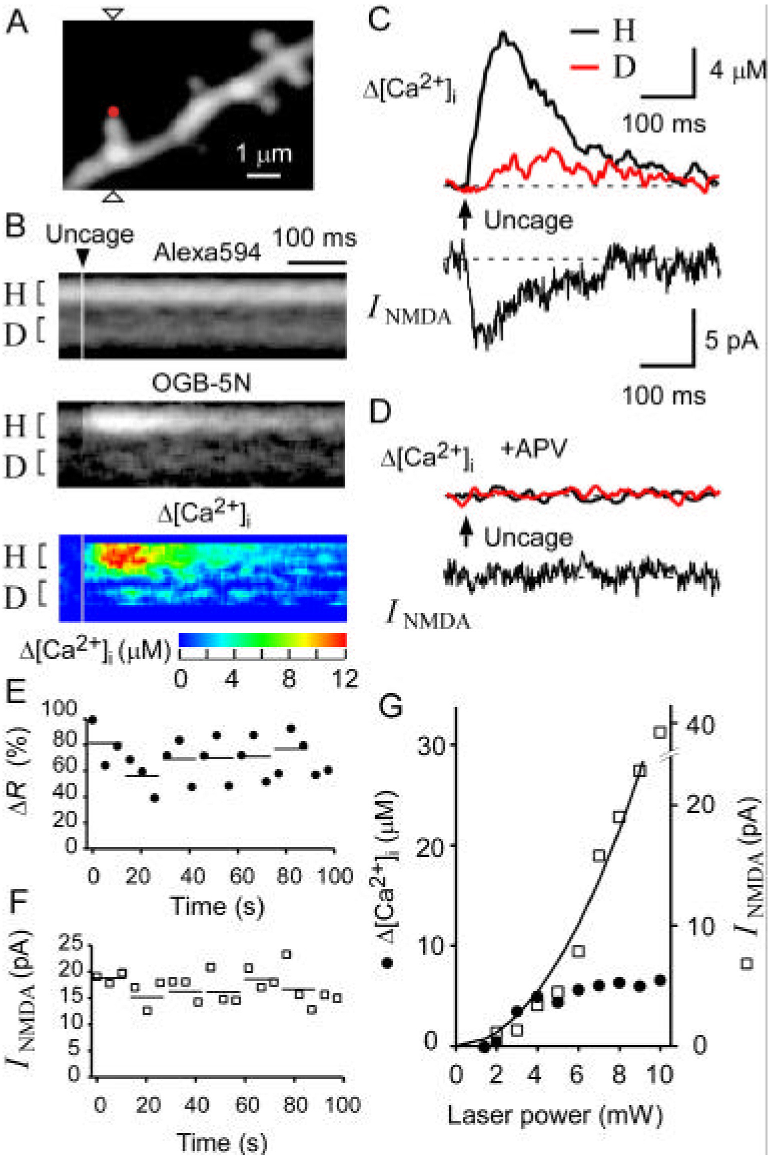

Figure 1. NMDAR-Mediated Ca^{2+} Signaling in Single Spines of CA1 Pyramidal Neurons in Response to Two-Photon Uncaging of MNI-Glutamate

(A) A three-dimensionally stacked two-photon fluorescence image of a region of a dendrite labeled with Alexa Fluor 594. Arrowheads indicate the line of laser scanning at 830 nm for fluorescence imaging, and the red dot represents the point of uncaging of MNI-glutamate.

(B) Line-scan images of the spine shown in (A) for Alexa Fluor 594 (top), OGB-5N (middle), and ?[Ca^{2+}]$_i$ obtained from the ratio of OGB-5N to Alexa Fluor 594 (bottom). The time of uncaging of MNI-glutamate is indicated by the arrowhead. The magnitude of ?[Ca^{2+}]$_i$ is pseudocolor coded as indicated.

(C) ?[Ca^{2+}]$_i$ in the spine head ("H") and at the base of the spine ("D") shown in (A) as well as NMDAR-mediated current (I_{NMDA}) recorded in the whole-cell patch-clamp mode. Regions of averaging of fluorescence to estimate ?[Ca^{2+}]$_i$ are indicated as "H" and "D" in (B).

(D) Elimination by APV (100 µM) of the [Ca^{2+}]$_i$ and I_{NMDA} responses to uncaging of MNI-glutamate in the neuron shown in (A).

(E and F) Stability of the maximal increase in the fluorescence ratio (?*R*) between OGB-5N and Alexa Fluor 594 (E) and of the maximal I_{NMDA} (F) in a spine head subjected to uncaging of MNI-glutamate for >20 times. Horizontal lines indicate averages of three consecutive amplitudes.

(G) Dependence of ?[Ca^{2+}]$_i$ and NMDAR-mediated current on the laser power for uncaging in a spine head with a volume of 0.12 µm^3

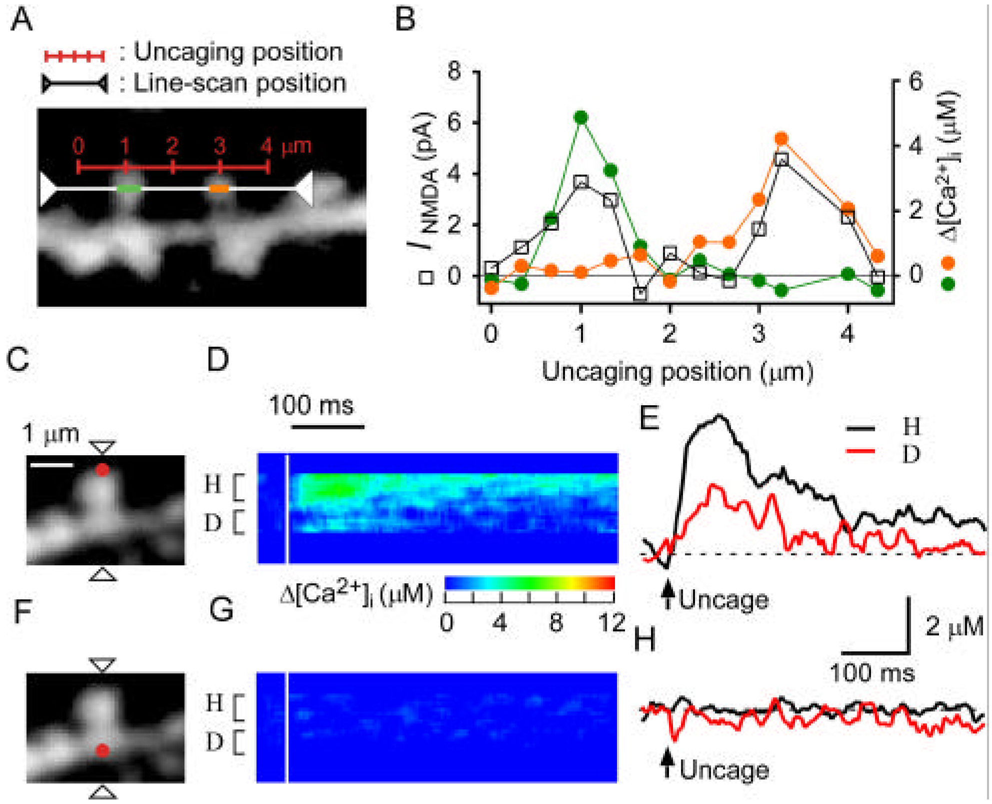

Figure 2. Spatial Spread of NMDAR Activation and of ?[Ca^{2+}]$_i$ in CA1 Pyramidal Neurons

(A) A stacked Alexa Fluor 594 image of a dendritic region. The red scale indicates the line along which uncaging of MNI-glutamate was sequentially induced, and the white line represents the scanning line for acquisition of fluorescence images.

(B) NMDAR-mediated current as well as ?[Ca^{2+}]$_i$ in the left (green circles) and right (orange circles) spines elicited by uncaging of MNI-glutamate at points along the red line in (A).

(C) Stacked Alexa Fluor 594 image of a spine for which line scanning was applied at the line indicated by the arrowheads and uncaging of MNI-glutamate was induced at the red spot.

(D and E) Line-scan images for ?[Ca^{2+}]$_i$ (D) and averaged traces of ?[Ca^{2+}]$_i$ (E) obtained from the spine shown in (C) during uncaging of MNI-glutamate at the red spot. Regions of averaging of fluorescence for ?[Ca^{2+}]$_i$ are indicated as "H" and "D" in (D).

(F–H) Panels corresponding to (C)–(E), respectively, for uncaging of MNI-glutamate at the position on the dendritic shaft indicated by the red dot in (F).

Dependence of the NMDAR-mediated response on spine structure

We induced uncaging of MNI-glutamate at spine heads that were separated from neighboring spines by >1.2 µm (unless the neighboring spines were much smaller than the selected spine) in order to record NMDAR-mediated currents that were attributable only to the identified spine (Figure 3A). Under these conditions, we were able to minimize the spillover effect on neighboring spines to <10% (Figure 2B). We measured the peak amplitude of I_{NMDA} (Figure 3B) as well as $\Delta[\mathrm{Ca}^{2+}]_i$ in the spine head (c_{H}) (Figure 3C) and in the dendritic shaft at the base of the spine (c_{D}) (Figure 3D) at the time when $\Delta[\mathrm{Ca}^{2+}]_i$ in the head was maximal (see Figure 10E). Data from four dendrites from different animals (41 spines in total) are summarized in Figure 3B–D. Our conclusions were also supported by data (not shown) from an additional 17 dendrites (213 spines in total). We found that the amplitude of I_{NMDA} correlated with spine-head volume (V_{H}), and this relation was most pronounced for spines on the same dendrite (Figure 3B), with the mean value ($\bar{r}$) of correlation coefficients being 0.48 for the four dendrites. A substantial I_{NMDA} was detected even in small spines, in contrast to the situation for AMPAR-mediated currents (see Figure 9G) (Matsuzaki et al., 2001). This observation was confirmed by the fact that a marked $\Delta[\mathrm{Ca}^{2+}]_i$ was detected in the head of most small spines (Figure 3C). In Figure 3, we were mainly concerned the diversity of spine parameters in each dendrite, since there was parametric variability among the dendrites to a certain degree (see Appendix, Spine Ca^{2+} model).

We found that c_{H} tended to be largest in spines with a small V_{H} ($\overline{r}$ = -0.50) (Figure 3C). A similar V_{H} dependence was previously observed for EPSCs evoked in CA1 pyramidal neurons by stimulation of presynaptic fibers (Nimchinsky et al., 2004). This inverse relation might be expected to be a direct consequence of a large spine volume giving rise to an increased rate of Ca^{2+} pumping or to increased dilution due to the reduced surface-to-volume ratio. However, several observations demonstrated that these explanations were not predominantly responsible for the inverse relation. First, if they were, c_{D} would be expected to show a V_{H} dependence similar to that of c_{H}, because Ca^{2+} efflux into the shaft would be proportional to c_{H}. We found, however, that c_{D} was actually greater for spines with a larger V_{H} ($\overline{r}$ = 0.48) (Figure 3D). Furthermore, a plot of the coupling ratio ($c_{\mathrm{R}} = c_{\mathrm{D}}/c_{\mathrm{H}}$) between c_{D} and c_{H} for each spine (Figure 3E) revealed that c_{R} was markedly dependent on V_{H}, with all values being <1, consistent with the notion that c_{D} reflects the outflow of Ca^{2+} from the spine head to the shaft (a c_{R} of >1 would imply the presence of a substantial number of extrasynaptic NMDARs). Similar V_{H} dependences of c_{H} and c_{R} were found in the presence of a blocker of the Ca^{2+} pump in the internal Ca^{2+} stores, cyclopiazonic acid (CPA, 30 µM) (Figure 4), indicating that the V_{H} dependences were due neither to Ca^{2+}-induced Ca^{2+} release (Emptage et al., 1999) nor to Ca^{2+} uptake into the internal Ca^{2+} stores (Majewska et al., 2000a).

The coupling ratio represents the efficiency of Ca^{2+} spread into the dendritic shaft, the major determinant of which would be expected to be the structure of the spine neck. We considered an equivalent circuit model of spine Ca^{2+} signaling under stationary conditions (see Figure 10C), given that $[Ca^{2+}]_i$ remained increased for >100 ms in response to uncaging of MNI-glutamate (see Discussion for time-dependent condition). The model predicts apparent flow of Ca^{2+} through the spine neck as

$$g_{\mathrm{N}}(c_{\mathrm{H}} - c_{\mathrm{D}}) = g_{\mathrm{D}} c_{\mathrm{D}} \tag{1}$$

where g_{N} and g_{D} are Ca^{2+} conductances of the spine neck and dendritic shaft, respectively (see “Spine Ca^{2+} model” in Appendix). It then follows that c_{R} relates directly to g_{N} as

$$g_{\mathrm{N}} = \frac{c_{\mathrm{D}}}{c_{\mathrm{H}} - c_{\mathrm{D}}} g_{\mathrm{D}} = \frac{c_{\mathrm{R}}}{1 - c_{\mathrm{R}}} g_{\mathrm{D}} \tag{2}$$

Indeed, we found that the coupling ratio was related to the structure of the spine neck as revealed by fluorescence images (see Figure 6A), with spines with shorter and thicker necks exhibiting larger coupling ratios. This observation implies that large spines tend to couple efficiently to the dendritic shaft as a result of a large neck conductance (g_{N}), and that clearance of Ca^{2+} along the dendritic shaft may result in a smaller c_{H} (see Figure 10A). In contrast, large and confined increases in $[Ca^{2+}]_i$ in small spines may be attributable to a small g_{N}.

Spine-neck geometry may therefore regulate the spread of spine Ca^{2+} signals, as was originally proposed for electrical signals in spines (Rall, 1970). To test this idea (see Figures 10A and 10B), we characterized the three major mechanisms of Ca^{2+} clearance from spine heads as reflected by g_{D}, g_{N}, and the Ca^{2+} conductance of the spine head (g_{H}).

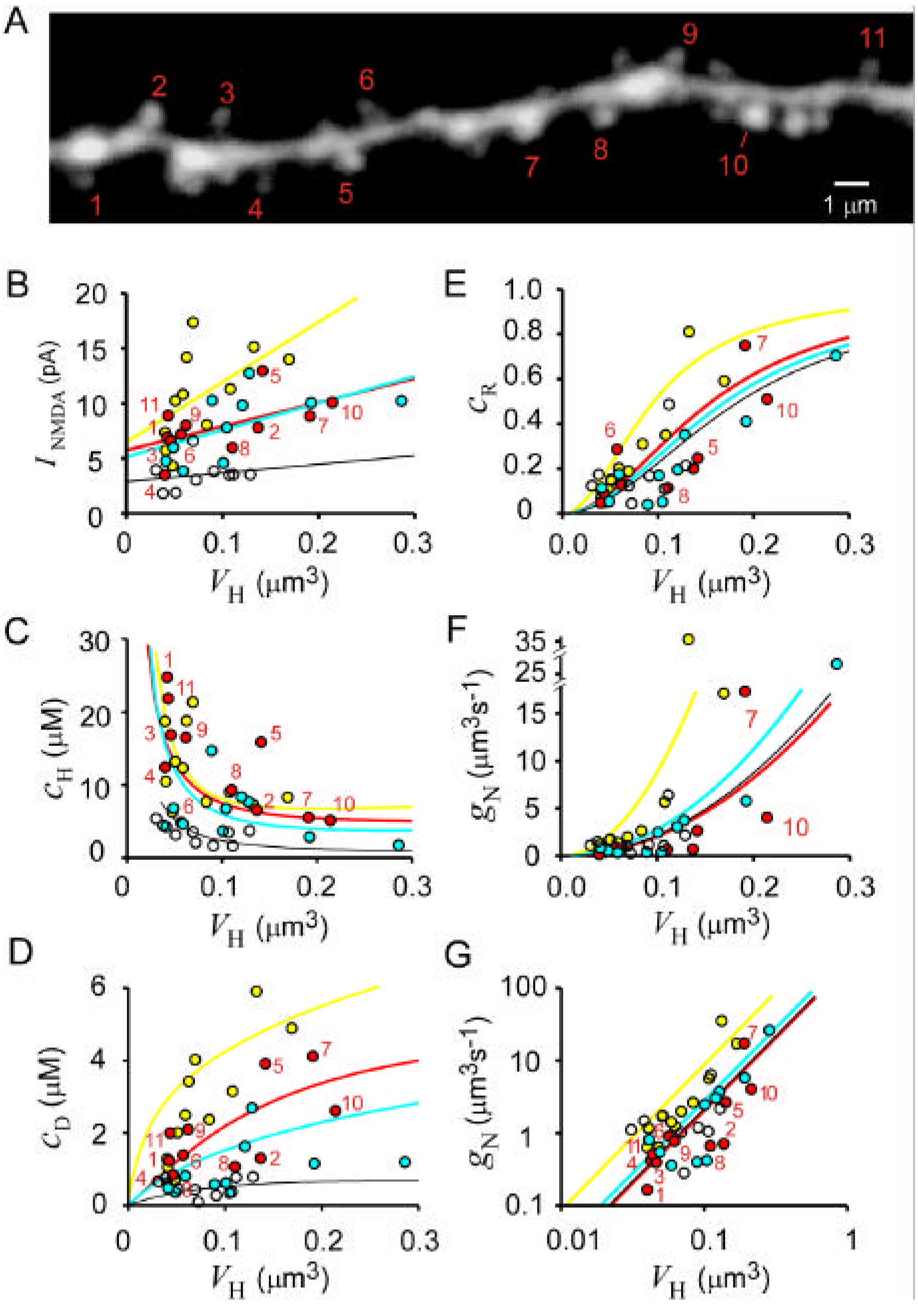

Figure 3. Dependence of NMDAR-Mediated Current and Ca^{2+} Signaling on Spine-Head Volume

(A) Stacked Alexa Fluor 594 image of a dendritic region in which uncaging of MNI-glutamate was induced at the numbered spines and line-scan imaging was performed along the axis of each spine. Original xy images are shown in **Appendix** (Figure 13**).**

(B–D) V_H dependence of NMDAR-mediated current (I_{NMDA}) (B) as well as of ?[Ca^{2+}]$_i$ in the spine head (c_H) (C) and in the dendritic shaft at the base of the spine (c_D) (D). Straight lines in (B) are linear regression lines. Uncaging was induced at the spines (red circles) indicated in (A) and at spines in three other dendrites (yellow, blue, and white circles). The amplitude of currents was measured at their peak, and ?[Ca^{2+}]$_i$ was measured at the time of the maximal value in spine heads.

(E) V_H dependence of the coupling ratio ($c_R = c_D/c_H$) for each spine.

(F and G) V_H dependence of Ca^{2+} conductance of the spine neck (g_N) and its double logarithmic plot, respectively. Smooth curves in (C)–(G) were drawn according to Equations 24–28 with four different sets of dendritic parameters as described in “Spine Ca^{2+} Model.”

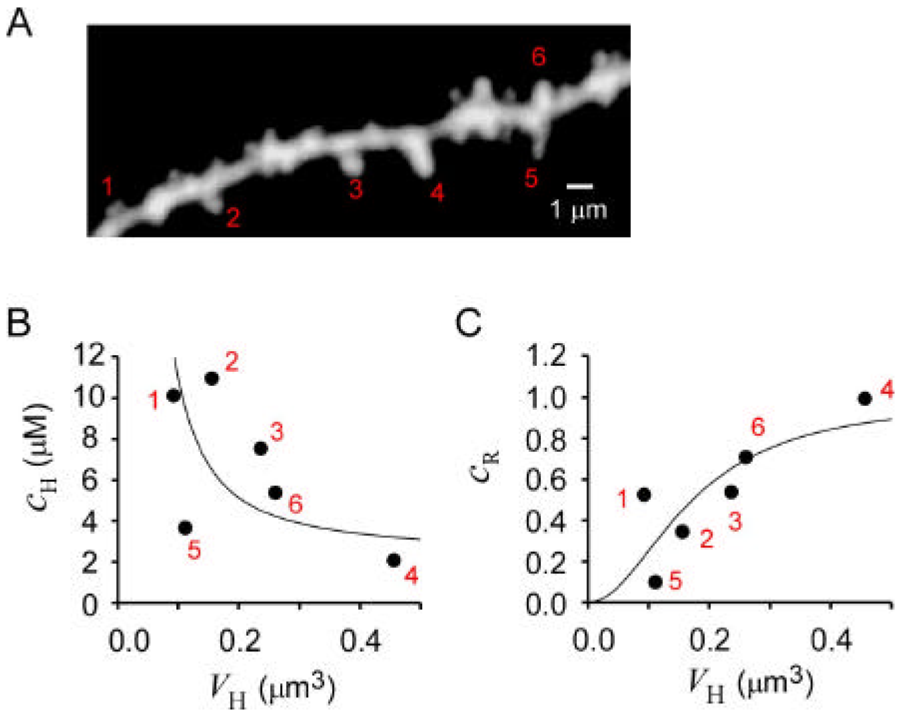

Figure 4. Dependence of NMDAR-Mediated Ca^{2+} Signaling on Spine-Head Volume in the Presence of Cyclopiazonic Acid (CPA, 30 μM)

CPA treatment abolished caffeine-induced Ca^{2+} release, and slowed the decay of NMDAR-mediated Ca^{2+} transients by 20% (data not shown).

(A) Stacked Alexa Fluor 594 image of a dendritic region in which uncaging of MNI-glutamate was induced at the numbered spines and line-scan imaging was performed along the axis of each spine.

(B and C) V_H dependence of $\Delta[Ca^{2+}]_i$ in the spine head (c_H) and the coupling ratio ($c_R = c_D/c_H$), respectively, for each spine. The correlation coefficients were –0.64 and 0.86 ($p < 0.027$, $n = 6$). Smooth curves were drawn according to Equations 26 and 28, respectively, with a set of parameters (g_D, t_H, a_0, a_1, a_N) as (10.5, 0.1, 39, 12, 354).

Ca^{2+} conductance of the dendritic shaft

To quantify g_D, we measured Ca^{2+} diffusion along a dendritic shaft by line scanning along the axis of the dendrite after stimulation of NMDARs of one spine by two-photon uncaging of MNI-glutamate (Figure 5A). Dendritic $[Ca^{2+}]_i$ remained at the plateau level for >100 ms (Figures 1C and 5B), suggesting that the distribution of Ca^{2+} along the dendrite was virtually stationary from 50 to 150 ms after uncaging. Indeed, the spatial distribution of Ca^{2+} along the shaft obtained at two different time points (Figure 5B, boxes 1 and 2) could be fitted by a single exponential function (Figure 5C) with similar length constants (λ = 1.6-1.9 µm). The dendritic λ ranged between 1.2 and 1.9 µm, with a mean value of 1.6 µm (*n* = 6). The input Ca^{2+} conductance of the dendritic shaft ($\mu m^3\ s^{-1}$) can be obtained in a manner analogous to that for the derivation of the input electrical conductance of axons (Johnston and Wu, 1995;Nicholls et al., 2001) as

$$g_D = (2\lambda\pi r_D^{\ 2})/\tau_D \qquad (3)$$

where τ_D and r_D are the time constant of $[Ca^{2+}]_i$ for and radius of the dendritic shaft, respectively [see Eq. (15)].

The value of τ_D was obtained from the decay of $[Ca^{2+}]_i$ after a sustained depolarization of neurons to –10 mV for 40 ms (Figure 5D). The decay was fitted by a single exponential function with a time constant ranging between 129 and 262 ms and with a mean value of 210 ms (*n* = 7). This mean value gave an estimate for g_D, defined by Equation (3), of $48r_D^2$ µm^3 s^{-1}. The mean ± SD diameter of dendrites in our preparations was 0.79 ± 0.15 µm (0.38 to 1.05 µm, $n = 41$), giving a mean g_D of ~7 µm^3 s^{-1}. These data yield an estimate for the apparent diffusion constant of Ca^{2+} in dendrites ($D_{app} = \lambda^2/\tau_D$) of 12 µm^2 s^{-1} [see Eq. (14)]. This value is similar to the estimates of D_{app} for intrinsic buffers (Allbritton et al., 1992;Gabso et al., 1997;Maeda et al., 1999), supporting that Ca^{2+} diffusion in the cytosol was not significantly affected by the usage of the Ca^{2+} indicator in our experimental conditions, where the Ca^{2+} binding ratio was raised only by 15.6 as relative to the intrinsic binding ratio of 86 (see below). Also, diffusion of Ca^{2+} indicators might be retarded in the cytosol (Kurebayashi et al., 1993;Gabso et al., 1997;Majewska et al., 2000a). It has recently been reported that CA1 pyramidal neurons show signfiicant expression of a diffusible high-affinity Ca^{2+} buffer, calbindin - D_{28K} (Muller et al., 2005), and D_{app} may be greater in the cells that are not whole-cell dialyzed.

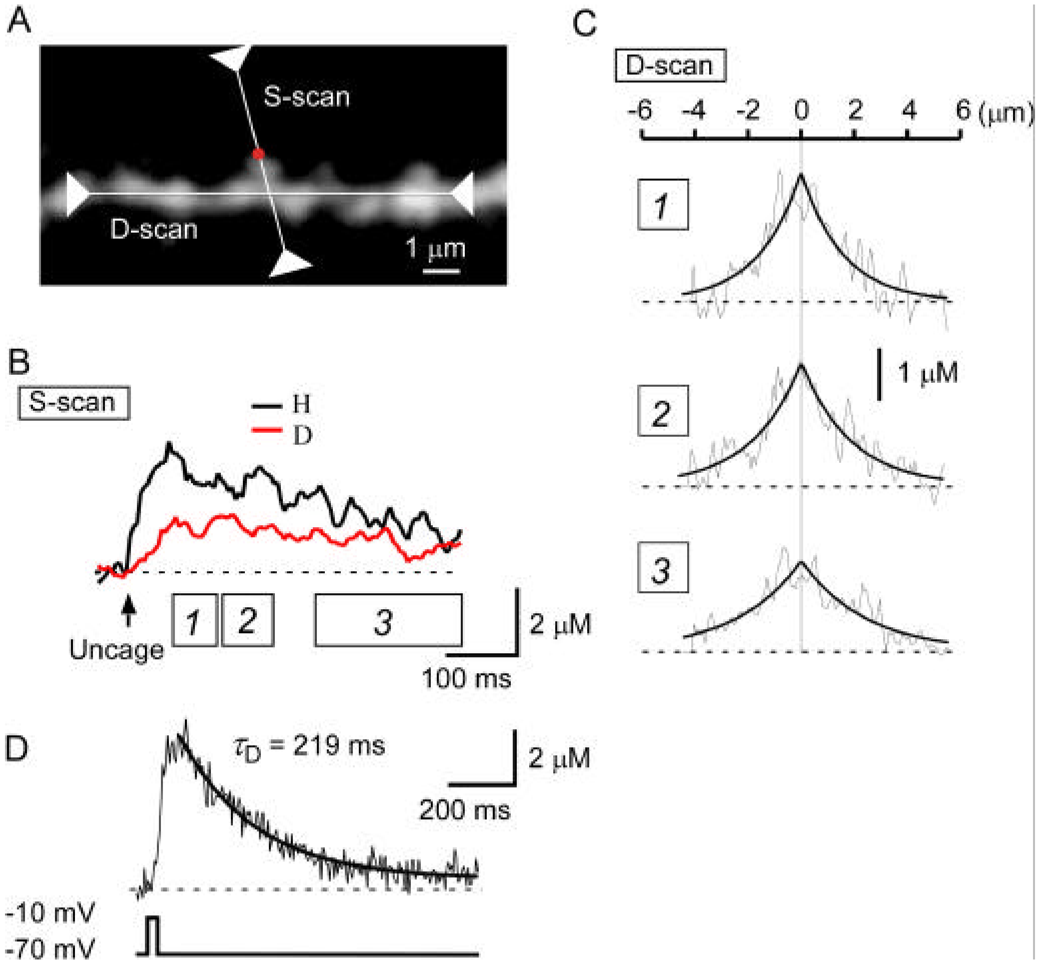

Figure 5. Spread of Ca^{2+} along the Axis of a Dendritic Shaft

(A) Stacked Alexa Fluor 594 fluorescence image of a dendritic region subjected to line scanning along both the axis of a spine (S-scan) and that of the parent dendritic shaft (D-scan). Uncaging of MNI-glutamate was performed at the position indicated by the red dot.

(B) Averaged ?[Ca^{2+}]$_i$ in the spine head (H) and at the base of the spine (D).

(C) Spatial gradient of ?[Ca^{2+}]$_i$ at three different time periods (boxes 1, 2, 3) depicted in (B). Smooth curves are exponential functions with length constants of 1.6 µm, 1.9 µm, and 2.4 µm for the periods 1, 2, and 3, respectively.

(D) Time course of ?[Ca^{2+}]$_i$ in a dendritic shaft whose soma was depolarized to -10 mV for 40 ms. The decay of ?[Ca^{2+}]$_i$ was fitted with an exponential curve with a time constant (t_D) of 219 ms.

Ca^{2+} conductance of the spine neck

We next estimated g_N based on Equation (2) with the use of the value of g_D estimated for a small region of the dendrite at the base of a spine (see “Spine geometries” in Materials and Methods). We found that g_N was highly related to V_H (Figure 3F). Neck conductance was small (<2 $\mu m^3\ s^{-1}$) when the spine-head volume was <0.1 μm^3 (Figure 3F), but it increased markedly in spines with head volumes of >0.1 μm^3. A double logarithmic plot (Figure 3G) revealed that g_N was roughly proportional to the second power of V_H. The values of g_N were similar to those of g_D, supporting the notion that Ca^{2+} diffusion through the spine neck can substantially affect $[Ca^{2+}]_i$ in the spine head.

The head-neck relation was confirmed by values of g_N (g_N*) estimated from fluorescence images of Alexa Fluor 594–labeled neurons according to the equation

$$g_N* = D_{app}\, p\, r_N^2 / (l_N + p\, r_N / 2) \tag{4}$$

where r_N and l_N represent the radius and length of the spine neck, respectively (Hille, 2001). Necks appeared dim and masked by the fluorescence of dendritic shafts and spine heads (Figure 6A), and we therefore corrected for background fluorescence as shown in Figure 6B and 6C (see Materials and Methods). For those stubby spines whose neck structures were not well resolved (Figure 6Ad), we assumed l_N as 0.05 μm and obtained r_N at the base of the spine. We found that the values of g_N were well correlated with those of g_N*, especially for spines on the same dendrite ($\bar{r}$ = 0.75)(r = 0.74, $P < 0.0001$, n = 39) (Figure 6D), despite the inherent imprecision in the estimates of g_N*. These data confirmed that g_N estimated from Ca^{2+} imaging did in fact reflect spine-neck geometry.

We found that g_N* also depended on the second power of V_H (Figure 6E), and that this relation was due to the correlation of V_H with both neck diameter (r = 0.7, $P < 0.001$, n = 32) and neck length (r = –0.54, $P < 0.0011$) (Figure 7). The ranges of neck diameter and length were similar to those determined by a previous analysis based on serial reconstruction of electron microscopic images (Harris et al., 1992). It has been difficult to analyze both spine-head volume and neck dimensions by electron microscopy, however, and the head-neck relation has not been previously demonstrated. In contrast, both the head volume and neck dimensions were readily determined both in our Ca^{2+}-imaging experiments and by our Alexa Fluor 594 fluorescence measurements. Estimation of g_N by Ca^{2+} imaging is likely to be especially reliable because it does not depend on the angle of spines with respect to the focal plane.

The head-neck relation was also maintained during structural plasticity associated with long-term potentiation (LTP) induced by repetitive uncaging of MNI-glutamate (Matsuzaki et al., 2004). We reexamined imaging data from our previous study and found that increases in g_N* were induced approximately in proportion to spine-head enlargement (r = 0.51, $P < 0.0013$) (Figure 11A). Indeed, the increase in g_N* was attributable predominantly to an increase in neck radius (r = 0.56, $P < 0.0004$, n = 35) (Figure 11B) rather than to a decrease in neck length ($r = -0.22$, $P = 0.21$) (Figure 11C), in contrast to previous proposals (Fifkova and Anderson, 1981;Crick, 1982).

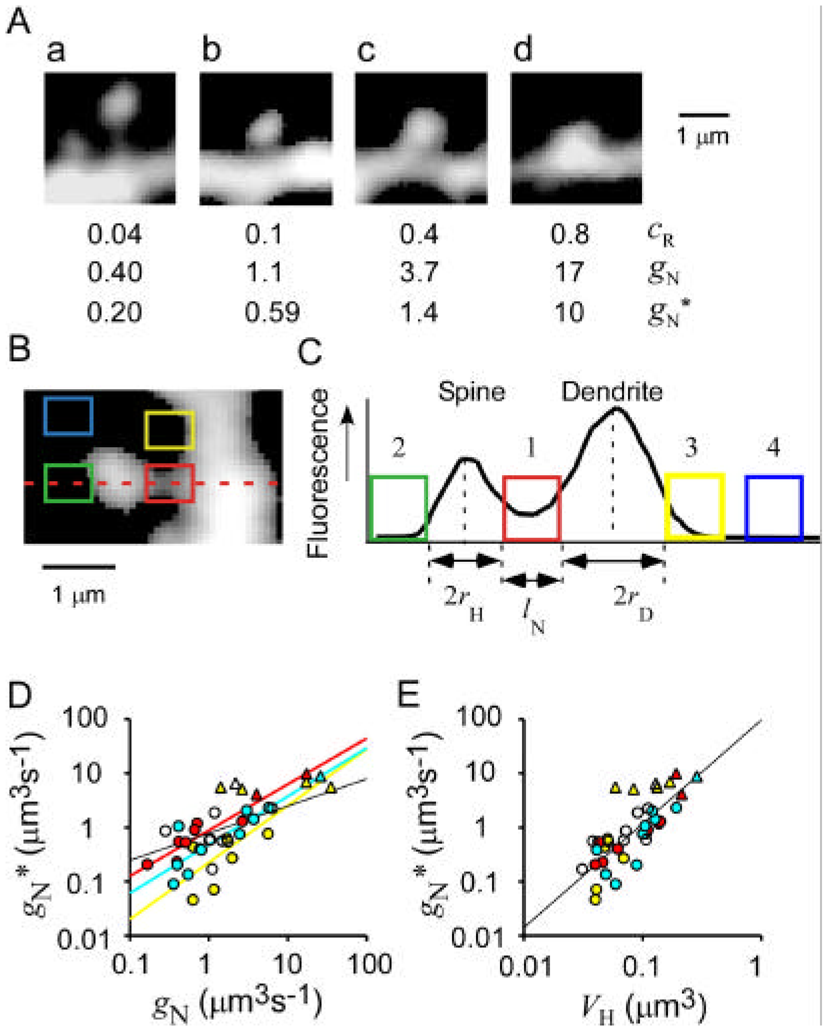

Figure 6. Spine-Neck Geometries

(A) Stacked Alexa Fluor 594 fluorescence images of dendritic spines with different c_R values. Necks appear to be shorter and thicker for spines with a larger c_R. Two values of spine-neck Ca^{2+} conductance, g_N and g_N*, were estimated from c_R and from fluorescence analysis as described below, respectively.

(B) Stacked Alexa Fluor 594 fluorescence image of a spine subjected to analysis of neck geometry.

(C) Fluorescence profile along the dashed line for the spine shown in (B). Four regions were selected for fluorescence measurement. The neck region (1) is flanked by the edges of the spine head and dendritic shaft, which are determined by curve fitting (see Materials and Methods). For those stubby spines whose neck structures were not well resolved, we assumed l_N as 0.05 µm and obtained r_N at the base of the spine. Regions of background fluorescence for the spine head (2) and the dendritic shaft (3) are placed at the predicted edge of a spherical spine and cylindrical shaft. A region of nonspecific background fluorescence (4) was positioned between 2 and 5 µm from the shaft.

(D) Relation between g_N* and g_N. Data obtained from the same dendrites are represented by the same colors as in Figure 3. We estimated g_N* from neck fluorescence according to Equation 4 and assuming D_{app} = 12 µm^2 s^{-1} (see Materials and Methods).

(E) Double logarithmic plot of the V_H dependence of g_N*. Straight lines in (D) and (E) are linear regression lines. Triangles in (D) and (E) indicate those stubby spines whose values of g_N* were obtained by assuming l_N = 0.05 µm.

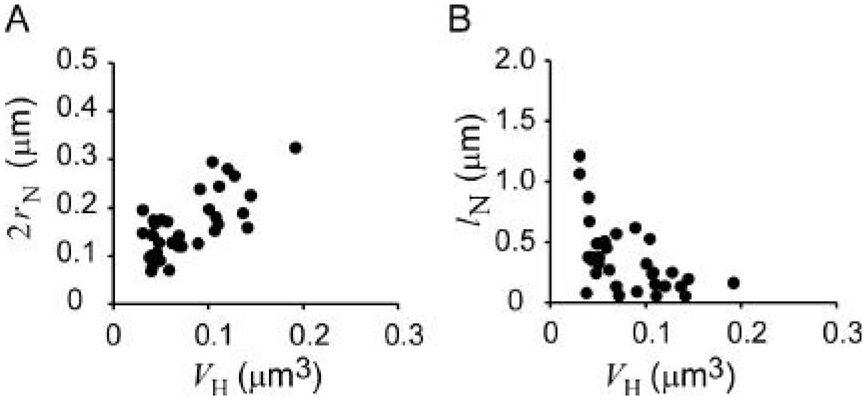

Figure 7. Spine-Neck Geometry underlying the Dependence of g_N on V_H^2

The V_H dependence of spine-neck diameter (A) and spine-neck length (B) was determined by analysis of Alexa Fluor 594 fluorescence images.

Ca^{2+} conductance of the spine head

Clearance of Ca^{2+} from the spine head is mediated both by Ca^{2+} diffusion through the spine neck (g_N) and by Ca^{2+} pumps in the spine head. We quantified the rate of Ca^{2+} pumping in terms of spine-head conductance (g_H) (see Figure 10C). For simplicity, we combined the effects of Ca^{2+} pumps in the Ca^{2+} stores and those in the plasma membrane, and we assumed that the capacity of pumping was proportional to both V_H and $[Ca^{2+}]_i$. The apparent Ca^{2+} clearance by Ca^{2+} pumps in the presence of Ca^{2+} buffers is then given by

$$V_H g_H c_H / k_T = (V_H / t_H) c_H = g_H c_H \qquad (5)$$

where γ_H and κ_T represent pump rate (s^{-1}) and total Ca^{2+} binding ratio (Neher and Augustine, 1992;Neher, 1995), respectively, and τ_H represents the time constant of the Ca^{2+} signal in the spine head ($\tau_H = \gamma_H / \kappa_T = V_H/g_H$). According to the definition of the Ca^{2+} binding ratio, κ_T can be estimated from

$$k_T \approx j_I / (V_H c_{IH}') \qquad (6)$$

where j_I and c_{IH}' represent molar Ca^{2+} flux at the peak of I_{NMDA} and the rate of increase in $[Ca^{2+}]_i$, respectively (see Figure 10E) [see Eq. (20)]. In the actual modeling, we corrected for the effect of Ca^{2+} pumping (g_H) and Ca^{2+} diffusion through the neck (g_N) with Equations (18) and (19). The values of κ_T thus obtained varied among spines (Figure 8A) because of errors in their estimation, but they were independent of V_H ($r = -0.24$, $P = 0.22$, $n = 27$) and the mean ± SD value was 102 ± 73. We thus estimated the intrinsic Ca^{2+} binding ratio of the spine head (κ) to be 86 (= 102 –16) in the whole-cell clamped neurons. The estimated value of κ is consistent with those (40 to 120) determined for many other cell types (Zhou and Neher, 1993;Helmchen et al., 1996;Maeda et al., 1999). In the same preparations, Sabatini et al. (2002) estimated κ to be 20; however, these researchers relied on population behavior of Ca^{2+}-decay kinetics among spines and they did not measure Ca^{2+} influx directly.

The value of g_H was then obtained from c_H, c_D, j_H (see Figure 10E), and κ_T according to our model (see Figure 10C):

$$g_H c_H = j_H / k_T - g_N (c_H - c_D) \tag{7}$$

where j_H represents Ca^{2+} influx at the peak of $\Delta[Ca^{2+}]_i$ in the spine head [see Eq. (19)]. We found that g_H was weakly proportional to V_H (r = 0.49, P = 0.002, n = 38) (Figure 8B), as expected from the relation $g_H = V_H/\tau_H$. The time constant of spine-head $[Ca^{2+}]_i$ estimated from $\tau_H = V_H/g_H$ was 0.05 ± 0.06 s (mean ± SD). This value is similar to a previous estimate of 0.014 s obtained from the time constant of decay of Ca^{2+} transients (Sabatini et al., 2002), taking into account the fact that we performed our experiments at room temperature (23° to 25°C) as opposed to 34°C in the previous study.

We found that g_N was as significant as was g_H in determining the spine Ca^{2+} signal, because values of g_N and g_H varied in a similar range and the ratio between g_N and g_H was scattered around a value of 1 (Figure 8C). This ratio was positively correlated with V_H ($r = 0.39$, $P < 0.015$, $n = 38$) (Figure 8C), reflecting the steeper V_H dependence of g_N (= $\alpha_N V_H^2$) (Figure 3G) relative to that of g_H (= V_H/τ_H). The smaller g_N of small spines thus contributes to a greater extent than does the lower rate of Ca^{2+} pumping (g_H) to the larger c_H (Figure 3C) and smaller c_D (Figure 3D) of these spines compared with those of larger spines. Consequently, Ca^{2+} pumping (g_H) is the major mechanism of Ca^{2+} clearance in certain spines with a small g_N, as was previously proposed (Sabatini et al., 2002). Such isolation of Ca^{2+} signals by the spine neck, however, was only partial in many spines (Figure 3E).

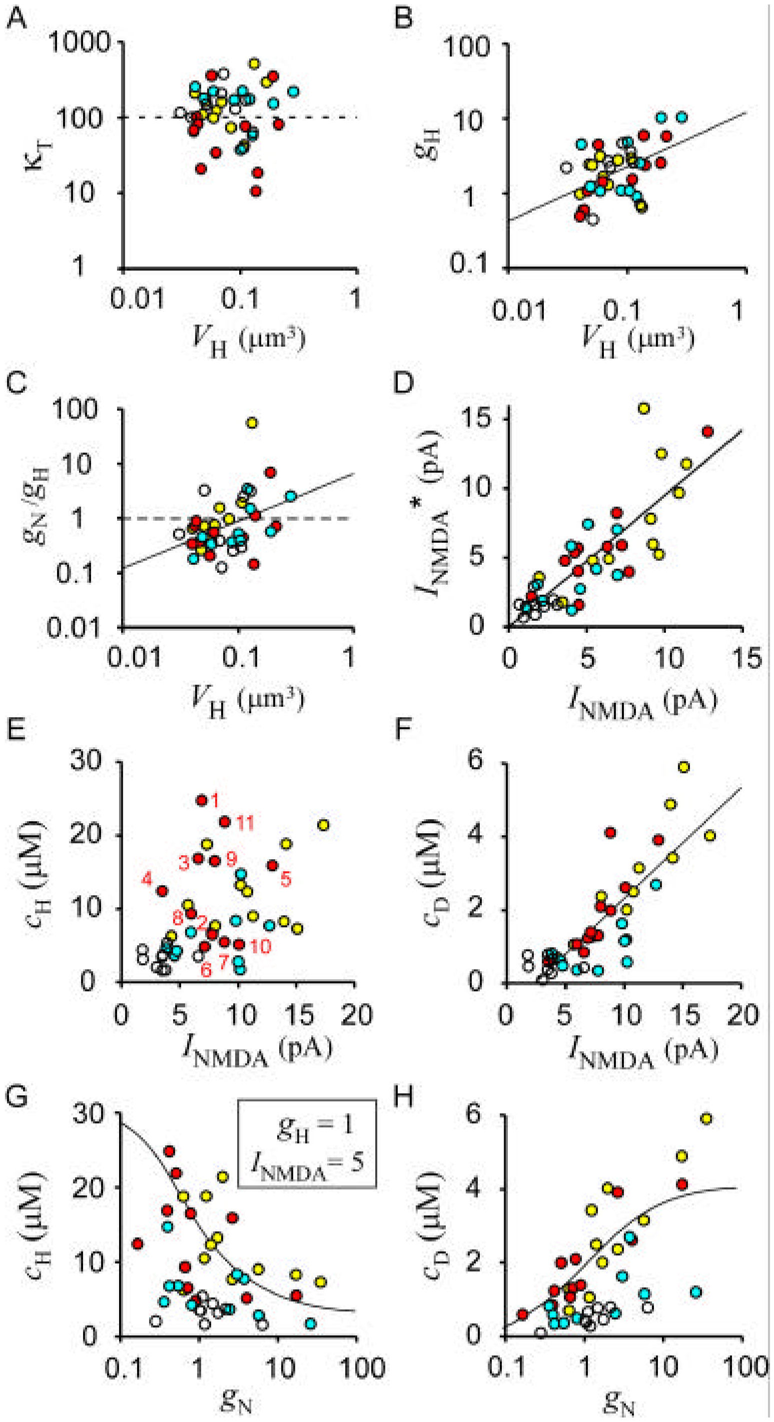

Figure 8. Determinants of Spine Ca^{2+} Signaling

(A and B) V_H dependence of ?$_T$ and g_H, respectively, among spines.

(C) V_H dependence of the g_N/g_H ratio.

(D) Predicted values of NMDAR-mediated current (I_{NMDA}*) from Equation 8 plotted against actual I_{NMDA} for each spine. Values of I_{NMDA} were obtained at the peak of spine [Ca^{2+}]$_i$ as shown in Figure 10E.

(E and F) I_{NMDA} dependence of c_H and c_D, respectively, among spines. Straight lines in (A)–(D) and (F) are linear regression lines.

(G and H) g_N dependence of c_H and c_D, respectively, among spines. Data obtained from the same dendrites are represented by the same colors as those in Figure 3. The smooth lines in (G) and (H) were obtained from Equations 21 and 22, respectively, assuming g_H = 1 µm^3 s^{-1}, g_D = 7 µm^3 s^{-1}, I_{NMDA} = 5 pA, ?$_T$ = 102, and g_N = 250 V_H^2.

Prediction of NMDAR-mediated current from Ca^{2+} imaging

To test the validity of our equivalent circuit model (see Figure 10C), we predicted NMDAR-mediated current from Ca^{2+}-imaging data and compared the predicted value with the actual whole-cell measurement of I_{NMDA}. Based on the model, we can predict the amplitude of NMDAR-mediated current (I_{NMDA}*) from measurement of c_{H} and c_{D} and the use of κ_{T}, g_{H}, and g_{D} as follows:

$$\frac{\varepsilon I_{\mathrm{NMDA}}{}^{*}}{2F\kappa_{\mathrm{T}}} = g_{\mathrm{H}}\, c_{\mathrm{H}} + g_{\mathrm{D}} c_{\mathrm{D}} \qquad (8)$$

where ε and F are the fractional Ca^{2+} current (Schneggenburger et al., 1993) mediated by the NMDAR and the Faraday constant, respectively [see Eq. (23)]. The predicted values (I_{NMDA}*) matched reasonably well with the actual values at the peak of spine $[Ca^{2+}]_i$ even with a fixed value (0.05 s) of τ_{H} (= $V_{\mathrm{H}}/g_{\mathrm{H}}$) ($r = 0.83$, $P < 0.0001$, $n = 41$) (Figure 8D). Remaining errors could be eliminated by adjusting τ_{H} between 0.01 and 0.2 s at each spine (data not shown). This analysis shows that our model accounts well for NMDAR-dependent Ca^{2+} signaling in dendrites.

Expression of AMPARs versus NMDARs

Finally, we analyzed the coexpression of NMDARs and AMPARs in the same spines. We first obtained a three-dimensional map of AMPAR-mediated current as described previously (Matsuzaki et al., 2001) by measurement of current in the presence of APV and in the absence of CNQX (Figure 9A–D). We then removed APV and measured NMDAR-mediated current evoked at the distal tip of spines in the presence of CNQX (Figures 9E and 9F). The level of AMPAR expression increased with spine size (*r* = 0.75, *n* = 31) (Figure 9G), consistent with our previous results (Matsuzaki et al., 2001). The spines that showed a higher level of expression of AMPARs also expressed a larger number of NMDARs (*r* = 0.73, *n* =31) (Figure 9H). As the spine-head volume increased, the AMPAR/NMDAR ratio also increased. Furthermore, a substantial number of NMDARs was present even in spines with a low level of AMPAR expression (Figure 9H).

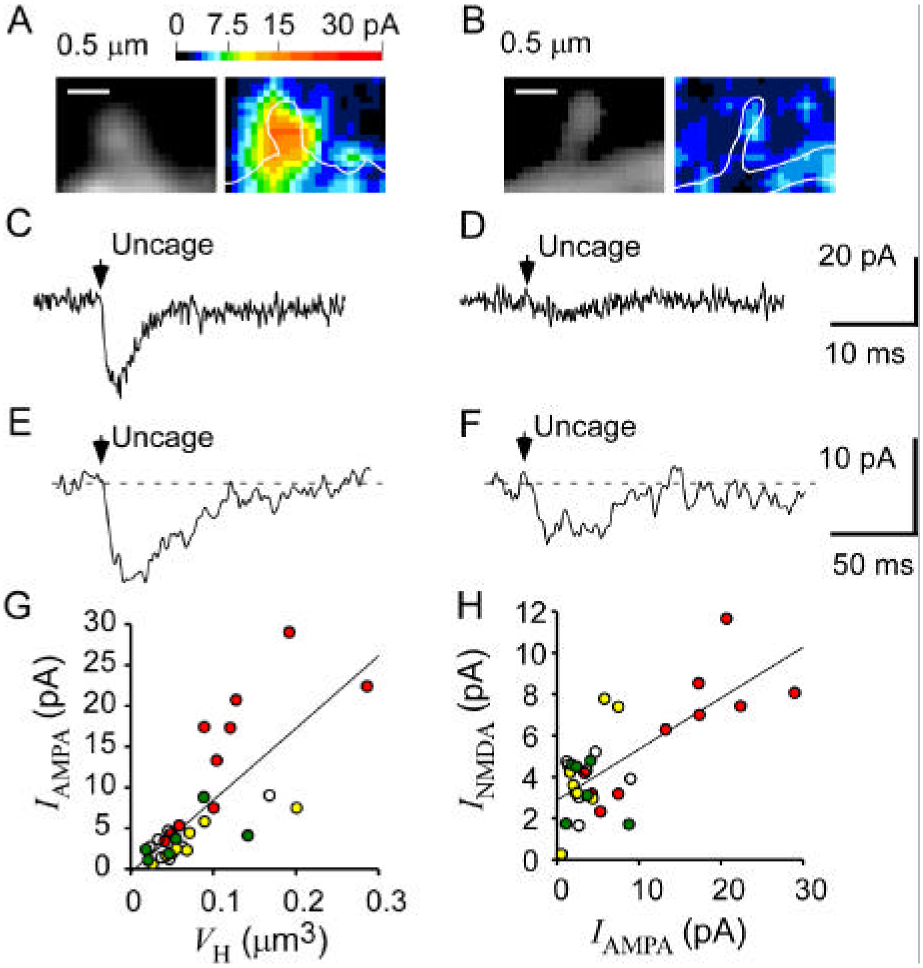

Figure 9. Functional Expression of AMPARs and NMDARs in the Same Spines

(A and B) Fluorescence images (left) of spines and their maps of AMPAR-mediated current (right). Current amplitude is pseudocolor coded as indicated.

(C and D) Maximal AMPAR-mediated currents in the spines shown in (A) and (B), respectively.

(E and F) NMDAR-mediated currents evoked by uncaging of MNI-glutamate at the tips of the spines show in (A) and (B), respectively.

(G) V_H dependence of the maximal AMPAR-mediated currents for 31 spines on four dendrites represented by different colors.

(H) Relation between the maximal amplitudes of NMDAR-mediated and AMPAR-mediated currents recorded from the same spines. Data in (G) and (H) were obtained from preparations different from those shown in Figure 3.

Discussion

We have systematically investigated the dependence of NMDAR-mediated Ca^{2+} signaling on spine geometry in hippocampal CA1 pyramidal neurons. Two-photon uncaging of MNI-glutamate allowed us to apply glutamate at any selected spine or dendritic surface and revealed a marked dependence of NMDAR-mediated Ca^{2+} signaling on spine geometry. The role of the spine neck in determining the fate of the Ca^{2+} signal, which we have clarified in the present study, is similar to the one originally proposed for attenuation of electrical signals by this structure (Rall, 1970); the spine neck was thus suggested to function physiologically to adjust the relative weights of synaptic inputs. Our data instead suggest that the spine neck determines the relative occurrence of Ca^{2+}-dependent synaptic plasticity at each spine.

Expression of NMDARs

We have found that all small spines manifest a substantial NMDAR-mediated current (I_{NMDA}). The extent of I_{AMPA} in small spines was less than that of I_{NMDA}, whereas the ratio of these currents changed markedly as the spine-head volume increased. Given that small spines have small postsynaptic densities (PSDs) (Harris and Stevens, 1989), our data suggest that NMDARs are anchored to small PSDs more effectively than are AMPARs, possibly as a result of direct binding of NMDARs to many PSD proteins—such as PSD95, α-actinin, Ca^{2+}- and calmodulin-dependent protein kinase II, and S-SCAM—that do not bind with high affinity to AMPARs (Sheng and Kim, 2002;Kasai et al., 2003). In addition, AMPARs may require a larger amount of F-actin for their efficient expression in PSDs (Kim and Lisman, 1999;Krucker et al., 2000). Thus, small spines might fulfill some of the criteria for “silent synapses” (Liao et al., 1995;Isaac et al., 1995;Durand et al., 1996). We detected small AMPAR-mediated currents even in small spines, however, suggesting that there are no strictly silent synapses, although we cannot exclude the possibility that such small currents were mediated by extrasynaptic receptors.

Our results provide the first direct demonstration that expression of functional NMDARs (I_{NMDA}) is correlated with spine-head volume (V_{H}). This finding is consistent with ultrastructural observations indicating that the amount of NMDAR immunoreactivity is correlated with the size of PSDs (Nusser et al., 1998), which is also correlated with V_{H} (Harris and Stevens, 1989). However, it has been difficult with traditional serial reconstruction techniques based on electron microscopy to demonstrate a direct positive correlation between spine-head volume and NMDAR density. We also found that I_{NMDA} was correlated with I_{AMPA} at the level of single spines, consistent with the electrophysiological demonstration that the amplitudes of AMPAR and NMDAR components of EPSCs are often highly correlated (Tyzio et al., 1999;Groc et al., 2002). The amplitudes of NMDAR-mediated currents were more variable than predicted, even though we averaged three current traces to reduce channel noise to a CV of 0.11, suggesting the operation of additional regulatory mechanisms of NMDAR expression other than that dependent on V_{H}.

The amplitude of I_{NMDA} showed only a weak correlation with spine-head $[\mathrm{Ca}^{2+}]_i$ within each dendrite (c_{H}, $\overline{r} = 0.18$) (Figure 8E). This apparent paradox is explained by the fact that the expected correlation between I_{NMDA} and c_{H} was canceled out by the positive correlation of I_{NMDA} with V_{H} and the negative correlation between V_{H} and c_{H} (Figure 10B). Large variability in c_{H}, even among spines with a similar I_{NMDA}, were explained by the diversity of spine structures: Spines 1, 7, and 9 in Figure 8E showed similar I_{NMDA} values, but their structures as reflected by V_{H} and g_{N} (especially g_{N}) were highly divergent (Figure 3G) in a manner that can account for the differences in c_{H} (Figure 10B). Thus, spine structure is as critical as is I_{NMDA} itself in determining c_{H}. It is possible that the expression of NMDARs is minimized in small spines to reduce c_{D} (Figure 8F), whereas spine structure determines the amplitude of c_{H} as necessary (Figure 10A, 8B).

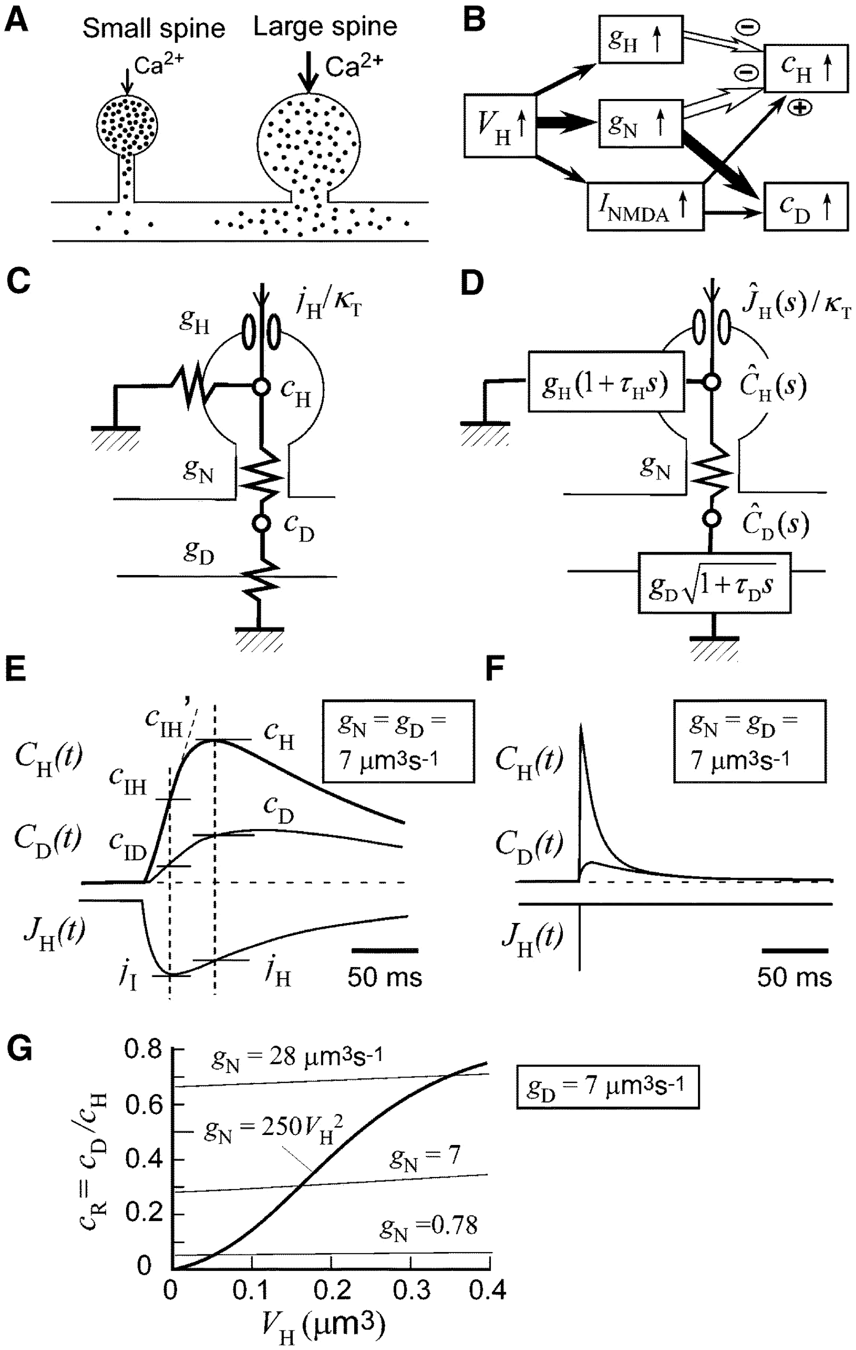

A
Small spine
Large spine
Ca2+
Ca2+
B
g_H ↑
c_H ↑
V_H ↑
g_N ↑
I_{NMDA} ↑
c_D ↑
⊖
⊖
⊕
C
j_H/κ_T
g_H
c_H
g_N
c_D
g_D
D
$\hat{J}_H(s)/\kappa_T$
$g_H(1+\tau_H s)$
$\hat{C}_H(s)$
g_N
$\hat{C}_D(s)$
$g_D\sqrt{1+\tau_D s}$
E
$C_H(t)$
$C_D(t)$
$J_H(t)$
c_{IH}'
c_{IH}
c_{ID}
c_H
c_D
j_I
j_H
$g_N = g_D =$ 7 μm3s-1
50 ms
F
$C_H(t)$
$C_D(t)$
$J_H(t)$
$g_N = g_D =$ 7 μm3s-1
50 ms
G
$c_R = c_D/c_H$
V_H (μm3)
0.8
0.6
0.4
0.2
0
0
0.1
0.2
0.3
0.4
g_N = 28 μm3s-1
$g_N = 250V_H^2$
g_N = 7
g_N =0.78
g_D = 7 μm3s-1

Figure 10. Spine Ca^{2+} Signals

(A) NMDAR-mediated influx of Ca^{2+} (dots) in small and large spines. The narrow neck of small spines results in larger and more confined increases in $[Ca^{2+}]_i$ in the spine head, allowing induction of LTP at the level of the single spine. The thick neck of large spines gives rise to smaller increases in spine $[Ca^{2+}]_i$ and greater outflow of Ca^{2+} into the dendritic shaft.

(B) Diagram showing the relative effects of spine-head volume (V_H) on spine-neck Ca^{2+} conductance (g_N), spine-head Ca^{2+} conductance (g_H), and I_{NMDA}, as well as of the latter parameters on spine-head $[Ca^{2+}]_i$ (c_H) and $[Ca^{2+}]_i$ in the dendritic shaft adjacent to the spine (c_D).

(C) Stationary model of Ca^{2+} signaling in a spine, where g_D, j_H, and $?_T$ represent Ca^{2+} conductance of the dendritic shaft, Ca^{2+} influx, and the total Ca^{2+} binding ratio, respectively.

(D) Time-dependent model, where t_H and t_D represent the time constants of $[Ca^{2+}]_i$ in the spine head and dendritic shaft, respectively. $J_H(s)$, $C_H(s)$, and $C_D(s)$ are the Laplace transforms of $J_H(t)$, $C_H(t)$, and $C_D(t)$, respectively, which represent the time courses of Ca^{2+} influx and of $[Ca^{2+}]_i$ in the spine head and in the dendritic shaft adjacent to the spine, respectively.

(E and F) Simulation of $C_H(t)$ and $C_D(t)$ based on the model in (D) and Equations 29 and 30, where $J_H(t)$ is either EPSC-like (E) or impulsive (F), and g_N, g_D, and g_H are all set to 7.0 $\mu m^3 s^{-1}$. As indicated in (E), c_H, c_D, and j_H are obtained at the time when $C_H(t)$ is maximal, and c_{IH}, c_{IH}', c_{ID}, and j_I are obtained at the time when $J_H(t)$ is maximal.

(G) V_H dependence of c_R (equal to c_D/c_H) in the time-dependent model in (D), where c_D and c_H are obtained as indicated in (E). The value of g_N is either fixed (thin lines) or V_H dependent (thick line). The values of g_D, t_D, t_H are set at 7 $\mu m^3 s^{-1}$, 0.2 s, 0.05 s, respectively, and g_H is altered according to V_H/t_H.

Spine head-neck relations

Our measurement of Ca^{2+} diffusion demonstrated that the Ca^{2+} conductance of the spine neck was highly dependent on spine-head volume (V_{H}), roughly in proportion to the second power of V_{H}. We have found that the spine neck is dynamically altered during the spine-head enlargement that underlies LTP (Matsuzaki et al., 2004), suggesting that the same mechanisms that sculpt the spine head also affect spine-neck conductance. Such spine head-neck relations appear to be preserved in individuals with mental retardation (Purpura, 1974;Fiala et al., 2002), particularly in those with fragile X syndrome (Hinton et al., 1991), in whom spines tend to have smaller heads and longer necks than in control individuals.

A similar tendency is present in the data of a study based on serial electron microscopic reconstruction, in spite of a large variability in the measurements (Harris et al., 1992). A weak positive correlation between spine-head volume and neck diameter as well as a negative correlation between neck length and neck diameter are thus apparent (Harris et al., 1992). In Golgi-stained preparations, spines with a large head (mushroom spines) also tend to have thicker necks than do thin spines (Peters and Kaiserman-Abramof, 1970). In contrast with morphological measurements, our functional measurement of neck Ca^{2+} conductance (g_{N}) provides an integrated index of the entire neck structure and has established the correlation between neck structure and head volume.

It should be noted, however, that the neck Ca^{2+} conductance was highly variable, differing by a factor of >10 even in spines with similar head volumes, and that V_{H} and g_{N} can be independently controlled to some extent. This finding is consistent with the existence of stubby and mushroom spines, although we could not determine a clear threshold value of g_{N} that delineates these two types of spine. Moreover, most spines could be grouped into one of three classes—thin, mushroom, and stubby—on the basis of both V_{H} and $g_{\mathrm{N}}*$ (Figure 11E), although there was no clear boundary between these designations. The three types of spine may thus simply reflect three extremes of one continuous population of spines. We detected typical mushroom spines with long narrow necks and large heads (filled stars in Figure 11E) in slice culture preparations, in which cells were allowed to recover fully from the injury inflicted by sectioning than we did in acute hippocampal slices. Although such spines diverged more markedly from the power relation $g_{\mathrm{N}} = a_{\mathrm{N}} V_{\mathrm{H}}^{2}$, they were relatively rare (3.5%, 4 out of 115 spines), and, on the whole, the correlation between V_{H} and $g_{\mathrm{N}}*$ in cultured slice preparations was steep and significant ($r = 0.55$, $P < 0.0001$, Figure 11E). It remains to be determined whether the same rule applies to other neurons and brain regions. It is possible that distinct relations between g_{N} and V_{H} contribute to neuron-specific regulation of spine structural plasticity.

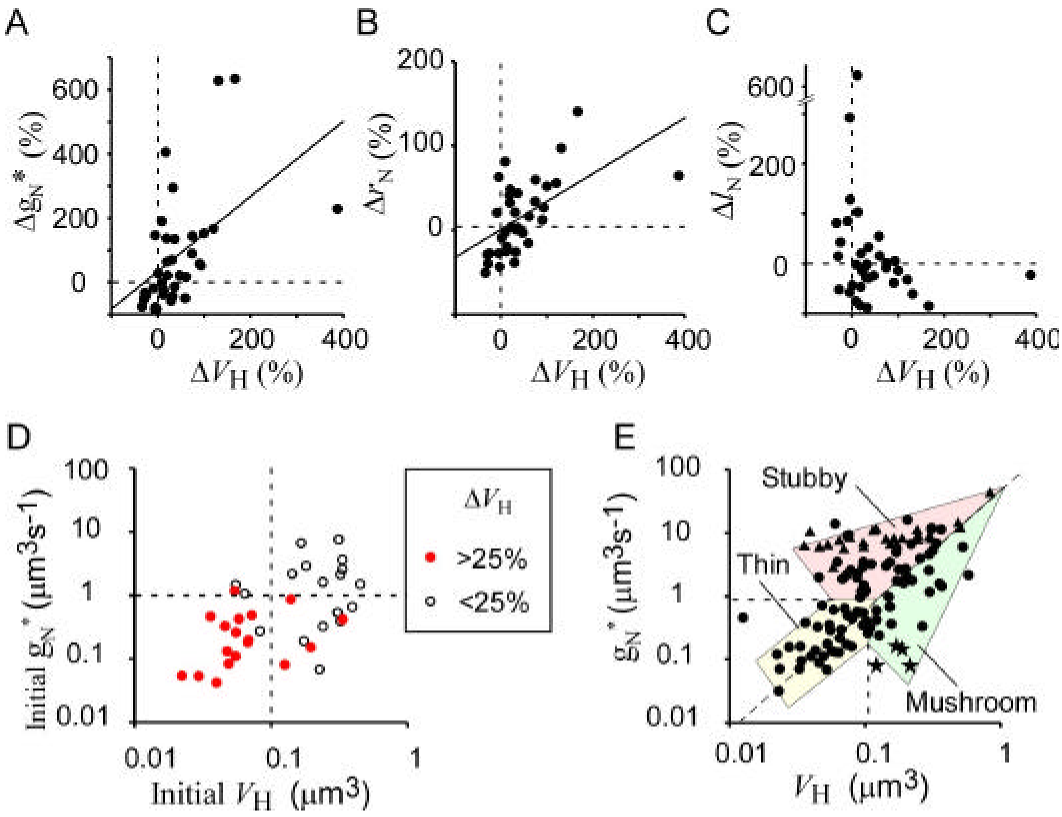

Figure 11. Spine-Neck Geometry during Plasticity and at Rest in Slice Culture Preparations Used in Our Previous Study (Matsuzaki et al., 2004)

(A–C) Proportional increases in g_N*, r_N, and l_N, respectively, versus those in V_H between before and after induction of long-lasting enlargement of spine heads by repetitive uncaging of MNI-glutamate. Values of g_N* were obtained assuming D_{app}=12 μm^2 s^{-1}.

(D) Dependence of long-lasting spine-head enlargement on both initial V_H and g_N*. Four out of 19 spines with an initial V_H of >0.1 μm^3 showed long-lasting head enlargement (>25%), but all these four spines exhibited an initial g_N* of <1.0. The same data set presented in our previous study (Supplemental Figure 2b of Matsuzaki et al., 2004) was reanalyzed in (A) through (D).

(E) Estimation of spine-neck Ca^{2+} conductance (g_N*) in 115 spines in 4 dendrites in slice culture preparations. The yellow, green and red regions contain thin, mushroom and stubby spines, respectively. Filled stars represent typical mushroom spines with long narrow necks and relatively large heads. Filled triangles indicate those stubby spines whose values of g_N* were obtained by assuming l_N = 0.05 μm.

Influence of the spine neck on dendritic Ca^{2+} signaling

The neck Ca^{2+} conductance (g_N) and head Ca^{2+} pumping (g_H) both play a role in isolation of spine Ca^{2+} signaling from the dendritic shaft and show a positive correlation with spine-head volume (V_H). However, we found that g_N is much more important than g_H in the control of c_H (Figure 10B). We thus showed that the V_H dependence and dynamic range of g_N were greater than those of g_H. Furthermore, the dependence of c_H and c_D on spine structure can be explained to a large extent by g_N, even assuming a constant g_H, in our model (Figure 8G and 8H). In contrast, if g_N is maintained constant, c_R would remain constant as V_H increases (Figure 10G). Finally, our model predicts that shaft $[Ca^{2+}]_i$ (c_D) approaches zero at $V_H = 0$ (Figure 3D) [see Eq. (27)] as a result of the steep (second power) V_H dependence of g_N. Thus, the dependence of g_N on $V_H{}^2$ plays a pivotal role in isolation of the Ca^{2+} signal in small spines.

In the foregoing analysis, we have assumed NMDAR-mediated Ca^{2+} influx to be stationary (Figure 10C), although it is actually time dependent (Figure 1C) as is the case with EPSCs. In the time-dependent condition, direct dilution of Ca^{2+} by the volumes of the spine head and dendritic shaft comes into play (Figure 10D). Our simulation, however, reveals that spine-neck geometry is also the pivotal factor for spine Ca^{2+} signaling in the time-dependent condition. First, the coupling ratio (c_R) does not depend markedly on V_H when g_N is held constant (Figure 10G) even in the EPSC-like model [Eqs. (29) and (30)]. This finding indicates that the steep V_H dependence of c_R in the EPSC-like condition also must be due to the V_H dependence of g_N. Second, shaft $[Ca^{2+}]_i$ (c_D) is reduced when Ca^{2+} influx is time dependent (Figures 10E and 10F). As far as the time integrals of increases in $[Ca^{2+}]_i$ are concerned, however, Equation (32) shows that the ratio between the time integral of the increase in head $[Ca^{2+}]_i$ and that of the increase in shaft $[Ca^{2+}]_i$ is exactly the same as c_R in the stationary condition. Third, the time integral of $C_H(t)$ depends on g_N in the same manner [Eq. (33)] as is apparent in the stationary condition [Eq. (21)], although the peak value of $C_H(t)$ is dependent only on V_H, not on g_N, in impulsive Ca^{2+} influx [Eq. (34)].

A rapid decay time constant (14 ms) for the Ca^{2+} signal in the spine head obtained in a previous study was attributed mostly to Ca^{2+} pumping (g_H) in the spine head, not to Ca^{2+} outflow (g_N) into the dendritic shaft (Sabatini et al., 2002). We calculate from this estimate that the head Ca^{2+} conductance ($g_H = V_H/\tau_H$) of a typical spine with a V_H of 0.05 µm^3 would be 3.6 µm^3 s^{-1}. If we assume a spine neck with typical dimensions of r_N = 0.1 µm and l_N = 0.2 µm, we can estimate, from Equation (4), that g_N is as large as 1.1 µm^3 s^{-1}, even assuming a moderate value of D_{app} of 12 µm^2 s^{-1} derived from our data. These calculations indicate that Ca^{2+} diffusion along the spine neck plays a substantial role in Ca^{2+} clearance in most spines, even assuming the large g_H found by Sabatini et al. (2002). Indeed, we detected a marked increase in shaft $[Ca^{2+}]_i$ for most spines under our experimental conditions, in which the Ca^{2+} binding ratio of the Ca^{2+} indicator was only 15.6, whereas the intrinsic Ca^{2+} binding ratio was estimated as 86. Sabatini et al. (2002) detected relatively small increases in the variance of shaft $[Ca^{2+}]_i$ (~20% of the variance of spine $[Ca^{2+}]_i$ in their Figure 4C and 4D) during back-propagating action potential–induced Ca^{2+} transients, and these were considered as evidence against diffusion of Ca^{2+} through the spine neck. The small increases in shaft noise, however, can be attributed to a large dilution effect of the dendritic shaft on impulsive Ca^{2+} influx (Figure 10F). It has been proposed using high-affinity Ca^{2+} indicators that there was a diffusional coupling between the spine head and dendritic shaft (Majewska et al., 2000a;Holthoff et al., 2002) and that spine elongation resulted in a better isolation of the spine Ca^{2+} signal (Majewska et al., 2000b;Korkotian et al., 2004).

The role of the spine neck in determination of Ca^{2+} signaling is similar to the one originally proposed for attenuation of electrical signals (Rall, 1970;Coss and Perkel, 1985). This latter notion was subsequently dismissed because of the diffusion of small molecules through the spine neck (Svoboda et al., 1996). We believe that our present data indicate that Rall's original idea deserves further consideration, given that we detected substantial expression of NMDARs even in small spines, which have a small neck conductance. The electrical conductance of the spine neck can be estimated from Equation (4) by replacing D_{app} with $1/\rho$, where ρ represents the specific resistance of the cytoplasm in the spine neck. If we assume $\rho = 100\ \Omega$ cm, the equation gives a value of 963 pS for the narrowest possible spine neck with a diameter of 0.05 µm and a length of 2 µm (Harris et al., 1992). The current flow into the dendrite would thus have been reduced by half assuming the opening of 50 channels with a single-channel conductance of 20 pS. This effect is predicted to be small for AMPARs, because they are expressed at a minimal level in small spines with a small g_{N} (Figure 9G). In contrast, expression of NMDARs is substantial in small spines, and NMDAR-mediated currents might indeed be electrically attenuated by narrow spine necks (Rall, 1970;Johnston and Wu, 1995). This attenuation might limit the infinitely large head $[\mathrm{Ca}^{2+}]_i$ (c_{H}) at small V_{H} that is predicted by Equation (26).

Spine necks and structural plasticity

Small spines have been found to be less stable than large spines in vivo (Grutzendler et al., 2002;Trachtenberg et al., 2002), and we have previously shown that small spines in slice preparations are the preferential sites for induction of long-term structural plasticity (Matsuzaki et al., 2004). We have now established that small spines tend to have narrow necks, which impede the efflux of Ca^{2+} into the dendritic shaft, and that this structural feature is the major contributing factor to the large, isolated increases in $[\mathrm{Ca}^{2+}]_i$ in small spine heads (Figure 10A). Their necks thus allow individual expression of LTP in small spines (Matsuzaki et al., 2004). Synaptic Ca^{2+} signaling in small spines appears to be optimized for selective induction of plasticity. In contrast, Ca^{2+} signaling in large spines appears to be optimized for smaller increases in head $[\mathrm{Ca}^{2+}]_i$ and larger increase in shaft $[\mathrm{Ca}^{2+}]_i$ (Figure 10A). Such Ca^{2+} efflux may contribute to synaptic plasticity, although its precise role remains to be determined. Spines actually exhibit a continuous structural distribution (Figure 3G; Figure 11E). Given that spine necks quantitatively regulate dendritic Ca^{2+} signals, they are likely important determinants of synaptic plasticity, which is bidirectionally regulated by Ca^{2+} signals (Lisman, 1989;Shouval et al., 2002).

The spine neck may also play a role in consolidation of spine structural plasticity. We have shown that large spines undergo marked enlargement during photochemical tetanus but that this morphological effect is not permanent (Matsuzaki et al., 2004), indicating that the consolidation of structural plasticity is impaired in large spines. This impairment cannot be attributed only to the smaller increases in $[Ca^{2+}]_i$ in such spines because many small spines showed similar increases (Figure 3C) yet their enlargement was long-lasting (Supplemental Figure 2b of Matsuzaki et al., 2004). We have now shown that spine-neck structure (g_N) is highly dependent on V_H. The impaired consolidation of enlargement of large spines can thus now be explained either by their large head volume or thick neck geometry (Figure 11D).

In summary, we propose that spine-head and spine-neck geometries play distinct roles in synaptic transmission and its plasticity, respectively. We have shown that the spine neck is the most important determinant of NMDAR-dependent Ca^{2+} signaling and Ca^{2+}-dependent synaptic plasticity, whereas the spine head determines synaptic transmission per se, given that spine-head volume is critical for expression of NMDARs (present study) and of

AMPARs (Matsuzaki et al., 2001;Matsuzaki et al., 2004) both in the steady-state and during plasticity.

Appendix

Spine Ca^{2+} model

We consider a single-compartment model of the dendritic spine in which Ca^{2+} enters through NMDARs and exits both through the action of Ca^{2+} pumps and by diffusion through a spine neck into a dendritic shaft of infinite length (Figure 10C). With the rapid buffer approximation (Neher, 1998;Maeda et al., 1999), the spatiotemporal distribution of [Ca^{2+}]$_i$ along the dendritic shaft [$C_D(x,t)$] with a uniform radius (r_D) can be described by

$$\frac{\partial C_D(x,t)}{\partial t} = D_{app}\frac{\partial^2 C_D(x,t)}{\partial x^2} - \frac{C_D(x,t)}{t_D} \tag{9}$$

where

$$D_{app} = (D_{Ca} + \sum_i k_i D_i)/k_T \tag{10}$$

and

$$k_T = 1 + \sum_i k_i \tag{11}$$

D_{Ca} represents the diffusion constant of Ca^{2+}, D_i and κ_i the diffusion constants and Ca^{2+} binding ratios of existing Ca^{2+} buffer molecules, and τ_D the time constant of [Ca^{2+}]$_i$ in the dendritic shaft. For simplicity, we assume [Ca^{2+}]$_i$ = 0 in the resting state. The spine is at $x = 0$, and we assume that Ca^{2+} flux is proportional to the difference between [Ca^{2+}]$_i$ in the spine head [$C_H(t)$] and that in the dendritic shaft [$C_D(0,t)$] and to the Ca^{2+} conductance of the spine neck [g_N, Eq. (4)]. We then have

$$-\pi r_{\mathrm{D}}^{2} D_{\mathrm{app}} \left. \frac{\partial C_{\mathrm{D}}(x,t)}{\partial x} \right|_{x \to +0} = \frac{g_{\mathrm{N}}(C_{\mathrm{H}}(t) - C_{\mathrm{D}}(0,t))}{2} \qquad (12)$$

In the stationary condition, Equation (9) gives

$$C_{\mathrm{D}}(x,t) = c_{\mathrm{D}}\, e^{-|x|/\lambda} \qquad (13)$$

with a length constant (µm) of

$$\lambda = \sqrt{D_{\mathrm{app}} \tau_{\mathrm{D}}} \qquad (14)$$

If we define dendritic-shaft conductance (µm^3 s^{-1}) as

$$g_{\mathrm{D}} = 2\pi \lambda r_{\mathrm{D}}^{2} / \tau_{\mathrm{D}} = 2\pi D_{app} r_{\mathrm{D}}^{2} / \lambda \qquad (15)$$

Equation (12) yields Equation (1) and

$$c_{\mathrm{D}} = c_{\mathrm{R}} c_{\mathrm{H}} = \frac{g_{\mathrm{N}}}{g_{\mathrm{N}} + g_{\mathrm{D}}} c_{\mathrm{H}} \qquad (16)$$

Amplitudes of NMDAR currents (I_{NMDA}) were converted to influx of Ca^{2+} into a volume of 1 µm^3 by $J = \frac{\varepsilon I_{\mathrm{NMDA}}}{2F}$ (M µm^3 s^{-1}), where F is the Faraday constant and ε the fractional Ca^{2+} current of NMDARs. In pyramidal neurons, ε was estimated as 0.107 (Garaschuk et al., 1996), which gives $\frac{\varepsilon}{2F}$ = 557 µM µm^3 s^{-1} pA^{-1}. For [Ca^{2+}]$_i$ in the spine head, $C_{\mathrm{H}}(t)$, we have

$$V_{\mathrm{H}} \frac{dC_{\mathrm{H}}(t)}{dt} = -g_{\mathrm{N}}(C_{\mathrm{H}}(t) - C_{\mathrm{D}}(0,t)) - g_{\mathrm{H}} C_{\mathrm{H}}(t) + \frac{J_{\mathrm{H}}(t)}{k_{\mathrm{T}}} \qquad (17)$$

The values of κ_{T} and g_{H} were estimated from the following two simultaneous equations derived from Equation (17):

$$V_{\mathrm{H}}\, c_{\mathrm{IH}}{}' = -g_{\mathrm{N}}(c_{\mathrm{IH}} - c_{\mathrm{ID}}) - g_{\mathrm{H}} c_{\mathrm{IH}} + \frac{j_{\mathrm{I}}}{k_{\mathrm{T}}} \qquad (18)$$

and

$$0 = -g_{\mathrm{N}}\,(c_{\mathrm{H}} - c_{\mathrm{D}}) - g_{\mathrm{H}} c_{\mathrm{H}} + \frac{j_{\mathrm{H}}}{k_{\mathrm{T}}} \qquad (19)$$

where c_{IH}', c_{IH}, c_{ID}, and j_{I} were obtained from traces at the peak of $J_{\mathrm{H}}(t)$, whereas c_{H}, c_{D}, and j_{H} were obtained at the peak of $C_{\mathrm{H}}(t)$ (Figure 10E). In the actual setting of the parameters,

$$k_{\mathrm{T}} \approx (j_{\mathrm{I}} - \frac{c_{\mathrm{IH}}}{c_{\mathrm{H}}} j_{\mathrm{H}})/(V_{\mathrm{H}}\, c_{\mathrm{IH}}{}') \;\approx\; j_{\mathrm{I}}/(V_{\mathrm{H}}\, c_{\mathrm{IH}}{}') \qquad (20)$$

When Ca^{2+} influx is stationary and $c = j_{\mathrm{H}}/k_{\mathrm{T}}$, Equations (1) and (19) yield

$$c_{\mathrm{H}} = \frac{g_{\mathrm{N}} + g_{\mathrm{D}}}{g_{\mathrm{H}}(g_{\mathrm{N}} + g_{\mathrm{D}}) + g_{\mathrm{N}} g_{\mathrm{D}}}\, c \qquad (21)$$

and

$$c_{\mathrm{D}} = \frac{g_{\mathrm{N}}}{g_{\mathrm{H}}(g_{\mathrm{N}} + g_{\mathrm{D}}) + g_{\mathrm{N}} g_{\mathrm{D}}}\, c \qquad (22)$$

Using Equations (16) and (21), we also have

$$c = g_{\mathrm{H}}\, c_{\mathrm{H}} + g_{\mathrm{D}} c_{\mathrm{D}} \qquad (23)$$

We found that spine-head volume (V_{H}) was related to the expression of NMDARs (Figure 3B) and spine-neck Ca^{2+} conductance (Figure 3G) as

$$c = a_0 + a_1 V_{\mathrm{H}} \qquad (24)$$

and $$g_{\mathrm{N}} = a_{\mathrm{N}} V_{\mathrm{H}}{}^{2} \tag{25}$$

respectively. With the use of these relations, the V_{H} dependence of c_{H}, c_{D}, and c_{R} was obtained from Equations (21), (22), and (16), as

$$c_{\mathrm{H}} = \frac{a_0 + a_1 V_{\mathrm{H}}}{\dfrac{V_{\mathrm{H}}}{t_{\mathrm{H}}} + \dfrac{1}{\dfrac{1}{g_{\mathrm{D}}} + \dfrac{1}{a_{\mathrm{N}} V_{\mathrm{H}}{}^{2}}}} \tag{26}$$

$$c_{\mathrm{D}} = \frac{a_0 + a_1 V_{\mathrm{H}}}{\dfrac{1}{t_{\mathrm{H}}}(V_{\mathrm{H}} + \dfrac{g_{\mathrm{D}}}{a_{\mathrm{N}} V_{\mathrm{H}}}) + g_{\mathrm{D}}} \tag{27}$$

and

$$c_{\mathrm{R}} = \frac{a_{\mathrm{N}} V_{\mathrm{H}}{}^{2}}{g_{\mathrm{D}} + a_{\mathrm{N}} V_{\mathrm{H}}{}^{2}} \tag{28}$$

Equations (24) to (28) fit well the actual data in Figure 3B through 3G, assuming a set of values (g_{D}, τ_{H}, α_0, α_1, α_{N}) as (5.02, 0.036, 17, 153, 206), (8.22, 0.066, 12, 93, 281), (8.03, 0.064, 28, 186, 883), and (7.5, 0.039, 8.8, 11.6, 219) for red, blue, yellow and white dendrites, respectively. The negative V_{H} dependence of c_{H} (Figure 3C) [Eq. (26)] could be attributed predominantly to the positive V_{H} dependence of g_{N} (Figure 3G) [Eq. (25), α_{N}] and g_{H} [Eq. (5)] as well as to the presence of NMDARs even in small spines (Figure 3B) [Eq. (24), α_0]. The positive V_{H} dependence of c_{D} (Figure 3D) [Eq. (27)] could be attributed to the positive V_{H} dependence of g_{N} [Eq. (25), α_{N}] and of I_{NMDA} (Figure 3B) [Eq. (24), α_1]. If g_{N} depends on a power of V_{H} of <2, c_{D} shows a nonzero positive value at

V_H close to 0, indicating that the V_H^2 dependence of g_N helps isolate the Ca^{2+} signal in small spines.

When Ca^{2+} influx is time dependent, the Laplace transformation of Equations (9), (12), and (17) yields the transforms of $C_\mathrm{H}(t)$ and $C_\mathrm{D}(t)$ as

$$\hat{C}_\mathrm{H}(s) = \frac{g_\mathrm{N} + g_\mathrm{D}\sqrt{1 + t_\mathrm{D}s}}{g_\mathrm{H}(1 + t_\mathrm{H}s)g_\mathrm{N} + (g_\mathrm{H}(1 + t_\mathrm{H}s) + g_\mathrm{N})g_\mathrm{D}\sqrt{1 + t_\mathrm{D}s}}\hat{C}(s) \tag{29}$$

and

$$\hat{C}_\mathrm{D}(s) = \hat{C}_\mathrm{R}(s)\hat{C}_\mathrm{H}(s) \tag{30}$$

respectively, where $\hat{C}(s)$ is the transform of $J_\mathrm{H}(t)/\kappa_\mathrm{T}$, and

$$\hat{C}_\mathrm{R}(s) = \frac{g_\mathrm{N}}{g_\mathrm{N} + g_\mathrm{D}\sqrt{1 + t_\mathrm{D}s}} \tag{31}$$

Given that $\hat{C}_\mathrm{D}(0) = \hat{C}_\mathrm{R}(0)\hat{C}_\mathrm{H}(0)$ and $\hat{f}(0) = \int_0^\infty f(t)dt$,

$$\int_0^\infty C_\mathrm{D}(t)dt = c_\mathrm{R}\int_0^\infty C_\mathrm{H}(t)dt \tag{32}$$

showing that the integrated $C_\mathrm{D}(t)$ and $C_\mathrm{H}(t)$ depend on spine structure exactly as in the stationary condition [Eq. (16)]. Similarly, Equation (29) gives

$$\int_0^\infty C_\mathrm{H}(t)dt = \frac{g_\mathrm{N} + g_\mathrm{D}}{g_\mathrm{H}(g_\mathrm{N} + g_\mathrm{D}) + g_\mathrm{N}g_\mathrm{D}}\int_0^\infty C(t)dt \tag{33}$$

indicating that integrated $C_\mathrm{H}(t)$ depends on g_N as does the stationary c_H [Eq. (21)]. The peak amplitude of $C_\mathrm{H}(t)$ for impulsive Ca^{2+} influx is determined by dilution due to spine-head volume (V_H), as Equation (29) gives

$$C_\mathrm{H}(0) = \hat{C}(\infty)/V_\mathrm{H} \tag{34}$$

To obtain time-dependent solutions, we analytically derived inverse Laplace transforms of $\hat{C}_{\mathrm{H}}(s)\hat{C}(s)$ or $\hat{C}_{\mathrm{D}}(s)\hat{C}(s)$ with Mathematica5.0 software. Numerical solutions were then calculated for an impulse response [$\hat{C}(s)=1$] (Figure 10F) and for an EPSC-like Ca^{2+} influx [$\hat{C}(s)=1.4c(\frac{1}{s+10}-\frac{1}{s+110})$] (Figure 10E, 10G). The factor 1.4 serves to adjust the peak amplitude of the influx as c. The value of g_{N} was either set constant, as indicated, or varied as g_{N} = 250 $V_{\mathrm{H}}{}^{2}$, whereas τ_{H} = 0.05 s and g_{D} = 7 µm^{3} s^{-1}. The time-dependent simulation revealed that values of c_{R} and g_{N} obtained from EPSC-like Ca^{2+} influx (Figure 10E) were less than the actual values by ~40% (Figure 10G), but we do not attempt to correct for this because it does not affect the conclusions of the present work.

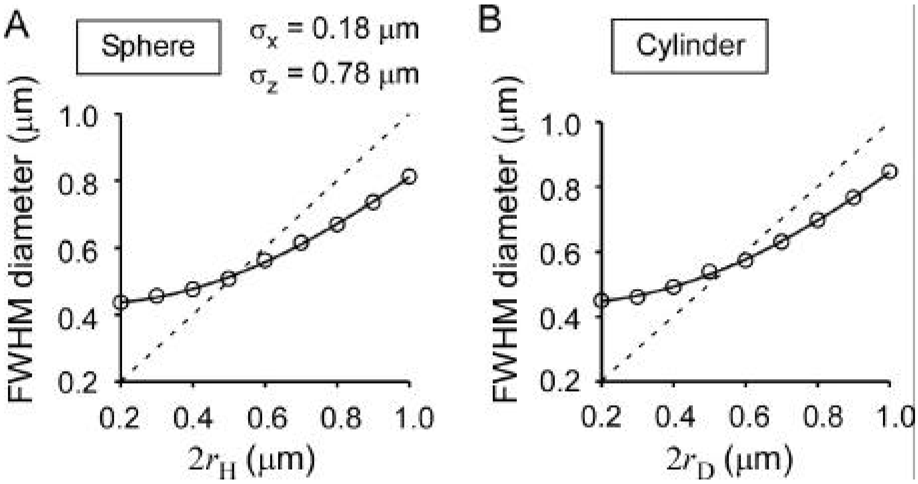

Figure 12. Actual and FWHM Diameters of Spheres and Cylinders

FWHM diameters of spheres (A) and cylinders (B) are plotted against actual diameters. The standard deviations of Gaussian approximation of the focal volume of two-photon excitation, s_x and s_z, were assumed to be 0.18 and 0.78 µm, respectively.

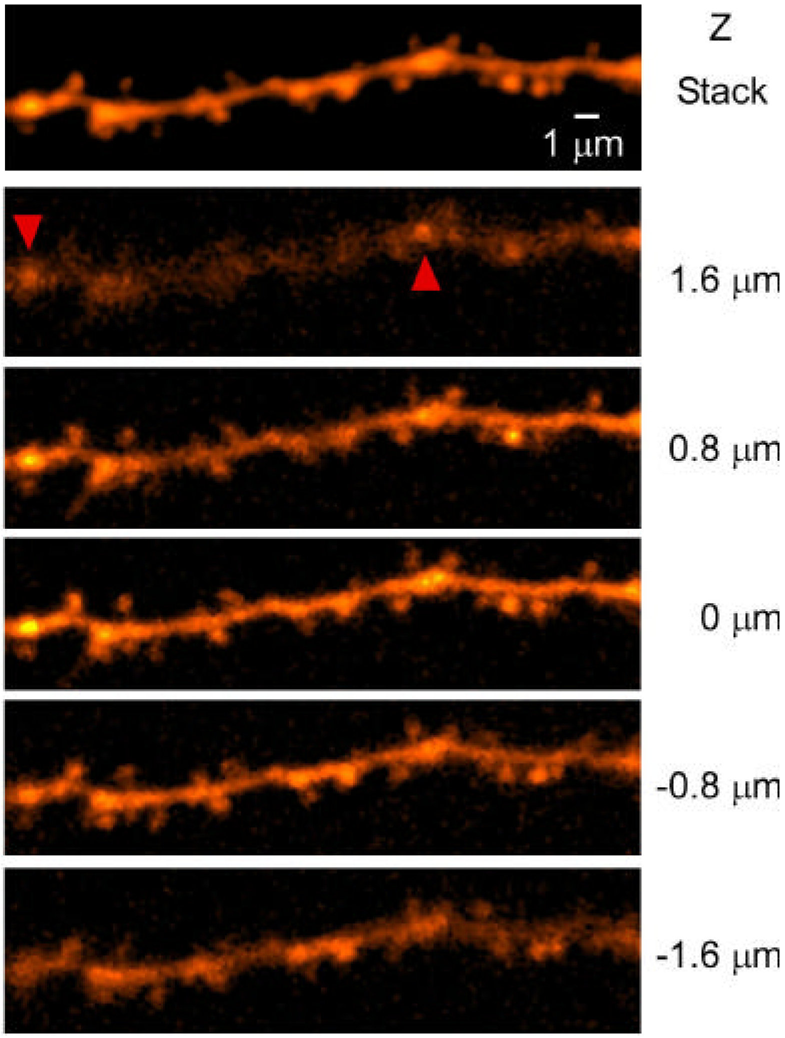

Figure 13. Original xy Images of the Dendrite Shown in Figure 3A

Arrowheads show the spines that were oriented along z-axis and that might appear swelling or beading of the dendritic shaft in the z-stacked image (Figure 3A).

Acknowledgments

I would like to extend my deepest thanks to Dr. Haruo Kasai and Dr. Masanori Matsuzaki for continuous and valuable guidance and discussion throughout this research. Also, I would like to express my sincere gratitude to Dr. Graham C. R. Ellis-Davies (Drexel Univ. College of Medicine) for cooperation throughout this study, Naoki Takahashi for his excellent programming and technical assistance, Dr. Tomomi Nemoto for many helpful suggestions, Dr. Kiyoshi Hama (National Institute for Physiological Sciences) for helpful comments on spine structure, Dr. Hajime Hirase (RIKEN brain science institute) for productive discussion, Tamaki Kise for various assistances, and all Kasai Lab members for helpful assistances and encouragements.

This work was supported by Grants-in-Aid from the Ministry of Education, Culture, Sports, Science, and Technology of Japan (H.K., M.M.) as well as by grants from the Human Frontier Science Program (G.C.R.E.-D., H.K.), NIH (G.C.R.E.-D., H.K.), NSF (G.C.R.E.-D), the Takeda Science Foundation (H.K.), and the McKnight Endowment Fund for Neuroscience (G.C.R.E.-D)..

References

Allbritton,N.L., Meyer,T., and Stryer,L. (1992). Range of messenger action of calcium ion and inositol 1,4,5-trisphosphate. Science *258*, 1812-1815.

Bonhoeffer,T., and Yuste,R. (2002). Spine motility. Phenomenology, mechanisms, and function. Neuron *35*, 1019-1027.

Coss,R.G., and Perkel,D.H. (1985). The function of dendritic spines: a review of theoretical issues. Behav. Neural Biol. *44*, 151-185.

Crick,F. (1982). Do dendritic spines twitch? Trends Neurosci. *5*, 44-46.

DiGregorio,D.A., and Vergara,J.L. (1997). Localized detection of action potential-induced presynaptic calcium transients at a Xenopus neuromuscular junction. J. Physiol. (Lond.) *505*, 585-592.

Durand,G.M., Kovalchuk,Y., and Konnerth,A. (1996). Long-term potentiation and functional synapse induction in developing hippocampus. Nature *381*, 71-75.

Emptage,N., Bliss,T.V., and Fine,A. (1999). Single synaptic events evoke NMDA receptor-mediated release of calcium from internal stores in hippocampal dendritic spines. Neuron *22*, 115-124.

Fiala,J.C., Spacek,J., and Harris,K.M. (2002). Dendritic spine pathology: cause or consequence of neurological disorders? Brain Res. Rev. *39*, 29-54.

Fifkova,E., and Anderson,C.L. (1981). Stimulation-induced changes in dimensions of stalks of dendritic spines in the dentate molecular layer. Exp. Neurol. *74*, 621-627.

Gabso,M., Neher,E., and Spira,M.E. (1997). Low mobility of the Ca^{2+} buffers in axons of cultured Aplysia neurons. Neuron *18*, 473-481.

Garaschuk,O., Schneggenburger,R., Schirra,C., Tempia,F., and Konnerth,A. (1996). Fractional Ca2+ currents through somatic and dendritic glutamate receptor channels of rat hippocampal CA1 pyramidal neurones. J. Physiol. (Lond.) *491*, 757-772.

Groc,L., Gustafsson,B., and Hanse,E. (2002). Spontaneous unitary synaptic activity in CA1 pyramidal neurons during early postnatal development: constant contribution of AMPA and NMDA receptors. J. Neurosci. *22*, 5552-5562.

Grutzendler,J., Kasthuri,N., and Gan,W.B. (2002). Long-term dendritic spine stability in the adult cortex. Nature *420*, 812-816.

Harris,K.M., Fiala,J.C., and Ostroff,L. (2003). Structural changes at dendritic spine synapses during long-term potentiation. Philos. Trans. R. Soc. Lond B Biol. Sci. *358*, 745-748.

Harris,K.M., Jensen,F.E., and Tsao,B. (1992). Three-dimensional structure of dendritic spines and synapses in rat hippocampus (CA1) at postnatal day 15 and adult ages: implications for the maturation of synaptic physiology and long-term potentiation. J. Neurosci. *12*, 2685-2705.

Harris,K.M., and Stevens,J.K. (1989). Dendritic spines of CA 1 pyramidal cells in the rat hippocampus: serial electron microscopy with reference to their biophysical characteristics. J. Neurosci. *9*, 2982-2997.

Helmchen,F. (2002). Raising the speed limit--fast Ca(2+) handling in dendritic spines. Trends Neurosci. *25*, 438-441.

Helmchen,F., Imoto,K., and Sakmann,B. (1996). Ca^{2+} buffering and action potential-evoked Ca^{2+} signaling in dendrites of pyramidal neurons. Biophys. J. *70*, 1069-1081.

Hille,B. (2001). Ion channels of excitable membranes (Sunderland, UK: Sinauer Associates).

Hinton,V.J., Brown,W.T., Wisniewski,K., and Rudelli,R.D. (1991). Analysis of neocortex in three males with the fragile X syndrome. Am. J. Med. Genet. *41*, 289-294.

Holthoff,K., Tsay,D., and Yuste,R. (2002). Calcium dynamics of spines depend on their dendritic location. Neuron *33*, 425-437.

Isaac,J.T., Nicoll,R.A., and Malenka,R.C. (1995). Evidence for silent synapses: implications for the expression of LTP. Neuron *15*, 427-434.

Johnston,D., and Wu,S.M.-S. (1995). Foundations of cellular neurophysiology (Boston: MIT press).

Kasai,H., Matsuzaki,M., Noguchi,J., Yasumatsu,N., and Nakahara,H. (2003). Structure-stability-function relationships of dendritic spines. Trends Neurosci. *26*, 360-368.

Kim,C.H., and Lisman,J.E. (1999). A role of actin filament in synaptic transmission and long-term potentiation. J. Neurosci. *19*, 4314-4324.

Koester,H.J., and Sakmann,B. (1998). Calcium dynamics in single spines during coincident pre- and postsynaptic activity depend on relative timing of back-propagating action potentials and subthreshold excitatory postsynaptic potentials. Proc. Natl. Acad. Sci. U. S. A. *95*, 9596-9601.

Korkotian,E., Holcman,D., and Segal,M. (2004). Dynamic regulation of spine-dendrite coupling in cultured hippocampal neurons. Eur. J. Neurosci. *20*, 2649-2663.

Kovalchuk,Y., Eilers,J., Lisman,J., and Konnerth,A. (2000). NMDA receptor-mediated subthreshold Ca(2+) signals in spines of hippocampal neurons. J. Neurosci. *20*, 1791-1799.

Krucker,T., Siggins,G.R., and Halpain,S. (2000). Dynamic actin filaments are required for stable long-term potentiation (LTP) in area CA1 of the hippocampus. Proc. Natl. Acad. Sci. U. S. A *97*, 6856-6861.

Kurebayashi,N., Harkins,A.B., and Baylor,S.M. (1993). Use of fura red as an intracellular calcium indicator in frog skeletal muscle fibers. Biophys. J. *64*, 1934-1960.

Lester,R.A., Tong,G., and Jahr,C.E. (1993). Interactions between the glycine and glutamate binding sites of the NMDA receptor. J. Neurosci. *13*, 1088-1096.

Liao,D., Hessler,N.A., and Malinow,R. (1995). Activation of postsynaptically silent synapses during pairing-induced LTP in CA1 region of hippocampal slice. Nature *375*, 400-404.

Lisman,J. (1989). A mechanism for the Hebb and the anti-Hebb processes underlying learning and memory. Proc. Natl. Acad. Sci. U. S. A *86*, 9574-9578.

Lisman,J. (2003). Long-term potentiation: outstanding questions and attempted synthesis. Philos. Trans. R. Soc. Lond B Biol. Sci. *358*, 829-842.

Maeda,H., Ellis-Davies,G.C., Ito,K., Miyashita,Y., and Kasai,H. (1999). Supralinear Ca2+ signaling by cooperative and mobile Ca2+ buffering in Purkinje neurons. Neuron *24*, 989-1002.

Majewska,A., Brown,E., Ross,J., and Yuste,R. (2000a). Mechanisms of calcium decay kinetics in hippocampal spines: role of spine calcium pumps and calcium diffusion through the spine neck in biochemical compartmentalization. J. Neurosci. *20*, 1722-1734.

Majewska,A., Tashiro,A., and Yuste,R. (2000b). Regulation of spine calcium dynamics by rapid spine motility. J. Neurosci. *20*, 8262-8268.

Matsuzaki,M., Ellis-Davies,G.C.R., Nemoto,T., Miyashita,Y., Iino,M., and Kasai,H. (2001). Dendritic spine geometry is critical for AMPA receptor expression in hippocampal CA1 pyramidal neurons. Nat. Neurosci. *4*, 1086-1092.

Matsuzaki,M., Honkura,N., Ellis-Davies,G.C., and Kasai,H. (2004). Structural basis of long-term potentiation in single dendritic spines. Nature *429*, 761-766.

Mori,H., and Mishina,M. (2003). Roles of diverse glutamate receptors in brain functions elucidated by subunit-specific and region-specific gene targeting. Life Sci. *74*, 329-336.

Muller, A., Kukley, M., Stausberg, P., Beck, H., Muller, W., and Dietrich, D. (2005). Endogenous Ca^{2+} buffer concentration and Ca^{2+} microdomains in hippocampal neurons. J. Neurosci. *25*, 558-565.

Nakazawa,K., McHugh,T.J., Wilson,M.A., and Tonegawa,S. (2004). NMDA receptors, place cells and hippocampal spatial memory. Nat. Rev Neurosci. *5*, 361-372.

Neher,E. (1998). Usefulness and limitations of linear approximations to the understanding of Ca^{++} signals. Cell Calcium *24*, 345-357.

Neher,E. (1995). The use of fura-2 for estimating Ca buffers and Ca fluxes. Neuropharmacology *34*, 1423-1442.

Neher,E., and Augustine,G.J. (1992). Calcium gradients and buffers in bovine chromaffin cells. J. Physiol. (Lond.) *450*, 273-301.

Nicholls,J.G., Martin,A.R., Wallace,B.G., and Fuchs,P.A. (2001). From Neuron to Brain (Sunderland, UK: Sinauer Associates).

Nimchinsky,E.A., Yasuda,R., Oertner,T.G., and Svoboda,K. (2004). The number of glutamate receptors opened by synaptic stimulation in single hippocampal spines. J. Neurosci. *24*, 2054-2064.

Nusser,Z., Lujan,R., Laube,G., Roberts,J.D., Molnar,E., and Somogyi,P. (1998). Cell type and pathway dependence of synaptic AMPA receptor number and variability in the hippocampus. Neuron *21*, 545-559.

Peters,A., and Kaiserman-Abramof,I.R. (1970). The small pyramidal neuron of the rat cerebral cortex. The perikaryon, dendrites and spines. Am. J. Anat. *127*, 321-355.

Petrozzino,J.J., Miller,L.D.P., and Connor,J.A. (1995). Micromolar Ca^{2+} transients in dendritic spines of hippocampal pyramidal neurons in brain slice. Neuron *14*, 1223-1231.

Purpura,D.P. (1974). Dendritic spine "dysgenesis" and mental retardation. Science *186*, 1126-1128.

Rall,W. (1970). Cable properties of dendrites and effects of synaptic location. In Excitatory synapic mechanisms, P. Andersen, and J.K.S. Jansen, eds. (Oslo: Universitetsforlaget), pp. 175-187.

Rusakov,D.A., and Kullmann,D.M. (1998). Extrasynaptic glutamate diffusion in the hippocampus: ultrastructural constraints, uptake, and receptor activation. J Neurosci *18*, 3158-3170.

Sabatini,B.L., Oertner,T.G., and Svoboda,K. (2002). The life cycle of Ca(2+) ions in dendritic spines. Neuron *33*, 439-452.

Schneggenburger,R., Zhou,Z., Konnerth,A., and Neher,E. (1993). Fractional contribution of calcium to the cation current through glutamate receptor channels. Neuron *11*, 133-143.

Sheng,M., and Kim,M.J. (2002). Postsynaptic signaling and plasticity mechanisms. Science *298*, 776-780.

Shepherd,G.M. (1996). The dendritic spine: a multifunctional integrative unit. J. Neurophysiol. *75*, 2197-2210.

Shouval,H.Z., Castellani,G.C., Blais,B.S., Yeung,L.C., and Cooper,L.N. (2002). Converging evidence for a simplified biophysical model of synaptic plasticity. Biol. Cybern. *87*, 383-391.

Svoboda,K., Tank,D.W., and Denk,W. (1996). Direct measurement of coupling between dendritic spines and shafts. Science *272*, 716-719.

Trachtenberg,J.T., Chen,B.E., Knott,G.W., Feng,G., Sanes,J.R., Welker,E., and Svoboda,K. (2002). Long-term in vivo imaging of experience-dependent synaptic plasticity in adult cortex. Nature *420*, 788-794.

Tyzio,R., Represa,A., Jorquera,I., Ben Ari,Y., Gozlan,H., and Aniksztejn,L. (1999). The establishment of GABAergic and glutamatergic synapses on CA1 pyramidal neurons is sequential and correlates with the development of the apical dendrite. J. Neurosci. *19*, 10372-10382.

Zhou,Z., and Neher,E. (1993). Mobile and immobile calcium buffers in bovine adrenal chromaffin cells. J. Physiol. (Lond.) *469*, 245-273.